Research in Astronomy and Astrophysics, 25:095014 (20pp), 2025 September
https://doi.org/10.1088/1674-4527/ade9e7
CSTR: 32081.14.RAA.ade9e7
© 2025. National Astronomical Observatories, CAS and IOP Publishing Ltd. All rights, including for text and data mining, AI training, and similar technologies, are reserved. Printed in China.

Broadband Spectral Analysis of 1ES 2344+514: A Multi-epoch Study

Kishor Chaudhury[1,2], Abhradeep Roy[3], Varsha R. Chitnis[3], Prajval Shastri[4], and Rajat K. Dey[2]
[1] Alipurduar University, Alipurduar, West Bengal 736122, India; chaudhurykishor@gmail.com
[2] University of North Bengal, Siliguri, Darjeeling, West Bengal 734013, India
[3] Tata Institute of Fundamental Research, Homi Bhabha Road, Colaba, Mumbai 400005, India
[4] Raman Research Institute, C. V. Raman Avenue, Sadashivanagar, Bengaluru 560080, India
Received 2024 December 21; revised 2025 June 11; accepted 2025 June 25; published 2025 July 30

Abstract

We present the results of the multi-epoch broadband spectral study of 1ES 2344+514 and study the evolution of physical parameters. We used nearly simultaneous data obtained from 2017 June 6 to 2022 August 6 (MJD 57910–59797) in optical, UV, X-ray and γ-ray wavebands from various instruments including Swift-UVOT, Swift-XRT, Nuclear Spectroscopic Telescope Array (NuSTAR), AstroSat (SXT and LAXPC), Fermi-LAT, and TeV flux from MAGIC. During 2017 July, 1ES 2344+514 appeared to be in the highest flaring state compared to other periods. We used the 0.5–7.0 keV and 3.0–20.0 keV data, respectively, from SXT and LAXPC of AstroSat and also 0.3–8.0 keV and 3.0–79.0 keV data, respectively, from Swift-XRT and NuSTAR. A joint fit between SXT and LAXPC, and between Swift-XRT and NuSTAR has been done for constraining the synchrotron peak. A clear shift in the synchrotron peak has been observed, which included 1ES 2344+514 in the HSP BL Lac family. A "harder-when-brighter" trend is observed in X-rays, and the opposite trend, i.e., "softer-when-brighter," is seen in the γ-rays. The multi-epoch broadband spectral energy distributions (SEDs) of this source were built and studied to get an idea of the radiation processes. The SEDs were fitted using a steady-state leptonic one-zone synchrotron+SSC model, and the fitted parameters of the emission region are consistent with those of other TeV BL Lacs. In this study, we found a weak correlation tendency between bolometric luminosity and magnetic field (B), as well as between bolometric luminosity and the break Lorentz factor ($\gamma_{\rm break}$).

Key words: galaxies: active – (galaxies:) BL Lacertae objects: individual (1ES 2344+514) – galaxies: jets – gamma-rays: galaxies – X-rays: galaxies

1. Introduction

Blazars are a subclass of accreting supermassive black holes (SMBHs) with relativistic jets that show high polarization and extreme variability at multiple frequencies on a range of timescales. This extreme behavior is understood to be a consequence of their relativistic jet being oriented at very close angles to the line of sight (e.g., Blandford & Königl 1979), and the non-thermal emission from the jet therefore dominating the total emission due to Doppler beaming. Blazars include Flat Spectrum Radio Quasars (FSRQs) that show prominent broad optical emission lines originating due to Keplerian gas clouds around the SMBH, and BL Lacertae objects (BL Lacs), which typically exhibit weak or no emission lines (Urry & Padovani 1995). Abdollahi et al. (2020) introduced the fourth Fermi-LAT AGN catalog (4FGL catalog), identifying 3137 blazars, 42 radio galaxies, and 28 other active galactic nuclei (AGNs) with detection significance above 4σ in the 50 MeV to 1 TeV energy range. Among this sample of blazars, 1131 were identified or associated with BL Lacs, 694 were identified or associated with FSRQs, and 1312 were blazar candidates of uncertain type. Analysis of Fermi-Large Area Telescope (LAT) observations reveals distinct differences between FSRQs and BL Lacs. Specifically, FSRQs exhibit softer gamma-ray spectra (photon spectral index (Γ) > 2.2, corresponding to energy spectral index > 1.2) and higher gamma-ray luminosities ($>10^{46}$ erg s^{-1}). In contrast, BL Lacs display harder gamma-ray spectra ($\Gamma < 2.2$ or energy spectral index <1.2) and lower luminosities (Ghisellini et al. 2009, 2010; Ackermann et al. 2011, 2015). Additionally, FSRQs demonstrate a "harder-when-brighter" tendency, whereas BL Lacs exhibit more diverse trends in γ-ray band. Low-frequency peaked (LSP) and intermediate-frequency peaked (ISP) BL Lacs often display a "harder-when-brighter" trend, while high-frequency peaked (HSP) BL Lacs tend to show "softer-when-brighter" patterns (Abdo et al. 2010c).

The spectral energy distributions (SEDs) in blazars exhibit a double-humped structure. The low-energy hump is located in the radio to X-ray bands, and the high-energy one is located in the γ-ray band. The production mechanism of broadband continuum spectra is commonly explained with two types of models: the leptonic model and the hadronic model. In both cases (FSRQs and BL Lacs), the low-energy hump of the SEDs is widely believed to be arising from the synchrotron radiation by relativistic electrons in the jet, occasionally

having significant contributions from the host galaxy thermal emission in the optical to infrared (IR) band (Urry & Padovani 1995). In the leptonic model, the high-energy hump is believed to be produced by inverse-Compton (IC) scattering of either synchrotron photons (known as synchrotron self-Compton (SSC; Maraschi et al. 1992; Krawczynski et al. 2004; Albert et al. 2007; Tavecchio et al. 2010; Aleksić et al. 2013)) or of low-energy photons from external regions like the accretion disk, broad-line region, torus (known as external Compton (EC) or external IC), or a combination of both (see, e.g., Dermer & Schlickeiser 1993; Sikora et al. 1994; Fan et al. 2006; Böttcher 2007; Abdo et al. 2010b; Ghisellini et al. 2010; Costamante et al. 2018). The spectral and variability differences between FSRQs and BL Lacs are attributed to distinct emission mechanisms, with FSRQs dominated by EC scattering and BL Lacs by SSC processes (Ghisellini et al. 2009, 2010). Alternatively, the origin of high-energy components of SEDs is also described using hadronic models via photo-meson production, neutral pion decay, and proton synchrotron radiation or synchrotron-pair cascading (see, e.g., Mannheim 1993; Aharonian 2000; Mücke & Protheroe 2001; Böttcher et al. 2013; Cerruti et al. 2015; Goswami et al. 2024). Based on the synchrotron peak frequency ($\nu_{\rm sp}$), blazars are subdivided into LSP ($\nu_{\rm sp} < 10^{14}$ Hz) blazars, ISP ($10^{14} < \nu_{\rm sp} < 10^{15}$ Hz) blazars, and HSP ($\nu_{\rm sp} \geqslant 10^{15}$ Hz) blazars (Abdo et al. 2010a; Padovani et al. 2017). Extreme high-frequency peaked (EHSPs) blazars, a subset of HSPs, have synchrotron peaks at $\nu_{\rm sp} \geqslant 10^{17}$ Hz and IC peaks typically at energies $\geqslant$1 TeV (Costamante et al. 2001; Aharonian et al. 2007; Acciari et al. 2010). Regarding jet composition of FSRQs and BL Lacs, FSRQ jets may be more magnetized, potentially Poynting-flux dominated, while BL Lac jets are likely less magnetized and particle dominated (Zhang et al. 2014; Tavecchio & Ghisellini 2016).

1ES 2344+514 (R.A. = $23^{\rm h}47^{\rm m}04\overset{\rm s}{.}837$, decl. = $+51^{\circ}42'17\overset{''}{.}878$, J2000) located at redshift $z = 0.044$ (Perlman et al. 1996) is a BL Lac. The estimated black hole mass of this object is $10^{(8.80\pm0.16)}\,M_{\odot}$ (Barth et al. 2003). It was first observed during the Einstein Slew Survey (Elvis et al. 1992) in the X-ray energy range (0.2–4 keV). It is also one of the extragalactic objects detected in the very-high-energy (VHE, >100 GeV) band. It was detected by the Whipple 10 m telescope at energies above 350 GeV during a bright flare of 1 day duration on 1995 December 20, with the flux level of ∼60% of the Crab Nebula (Catanese et al. 1998; Schroedter et al. 2005). Strong variability, with a factor of ∼2 variations in 2–10 keV flux, was observed with BeppoSAX in 1996 December on a timescale of about 5 ks during the flaring state (Giommi et al. 2000). Later, 1ES 2344+514 was also observed by Swift in the X-ray band in 2005 on various occasions, with its 2–10 keV flux steady around 1×10^{-11} erg cm^{-2} s^{-1}, which is lower than the flux measured in 1996 December (Tramacere et al. 2007). Kapanadze et al. (2017) reported that during the monitoring campaign with Swift during 2005–2015, the source showed high variability on longer timescales (weeks to months) with the 0.3–10 keV flux varying by a factor of 13.3. 1ES 2344+514 has been studied through Fermi-LAT observations, revealing its gamma-ray characteristics and variability, such as a low flux state in 2008 (Aleksić et al. 2013) and an enhanced state in 2016 (MAGIC Collaboration et al. 2020) with a flux of approximately 1.2×10^{-8} cm^{-2} s^{-1} in the 0.3–300 GeV range, as noted in multi-wavelength campaigns. No significant flaring activity was found in the VHE γ-ray band with the Very Energetic Radiation Imaging Telescope Array System (VERITAS) between 2007 and 2015, which corresponds to the quiescent state of 1ES 2344+514 in VHE (Allen et al. 2017). Multiwavelength studies of the source have been carried out using simultaneous and quasi-simultaneous data, and the SEDs were modeled on a few occasions (Albert et al. 2007; Godambe et al. 2007; Acciari et al. 2011; Aleksić et al. 2013; MAGIC Collaboration et al. 2020). MAGIC Collaboration et al. (2020) reported that 1ES 2344+514 was detected in a high flaring state in VHE γ-rays during 2016 August by ground-based γ-ray telescopes, including the First G-APD Cherenkov Telescope (FACT) and the Major Atmospheric Gamma Imaging Cherenkov Telescopes (MAGIC), and observed that the synchrotron peak shifted to frequencies exceeding 10^{18} Hz. Also, the peak of the synchrotron emission was found near frequencies of the order of $\approx 10^{16}$–10^{17} Hz during the quiescent state (Giommi et al. 2000; Aleksić et al. 2013; Nilsson et al. 2018; MAGIC Collaboration et al. 2024).

In this paper, we report the simultaneous and quasi-simultaneous observations of 1ES 2344+514 from 2017 to 2022, in optical, ultraviolet (UV), X-ray and γ-ray bands. We present the results of individual and joint spectral fittings covering soft and hard X-rays. We used the data in optical, UV, X-ray and γ-ray bands for a multiwavelength study to understand the broadband properties of the source. The SED in different epochs has also been constructed and fitted with the two-component and one-zone synchrotron+SSC model. The paper is structured as follows: In Section 2 of this paper, we describe the details of the instruments used for multiwavelength observations, procedures for data reduction, and analysis. In Section 3, we present the results of this analysis. Details of the SED modeling along with results are discussed in Section 4. We present the discussion in Section 5, and finally, the conclusions are listed in Section 6.

2. Multiwavelength Observations, Data Reduction and Data Analysis

1ES 2344+514 was observed on several occasions in the X-ray band with the Soft X-ray Telescope (SXT) and Large Area X-ray Proportional Counter (LAXPC) onboard AstroSat[5] (Singh et al. 2014), X-Ray Telescope (XRT) onboard Neil Gehrels Swift Observatory (Burrows et al. 2004) and Nuclear

[5] https://www.isro.gov.in/AstroSat.html

Table 1
X-Ray, UV, and Optical Observations of 1ES 2344+514

Instrument	Energy Band (keV)	Obs. Id	Start Time YYYY-MM-DD HH:MM:SS	Stop Time YYYY-MM-DD HH:MM:SS	Exposure Time (s)	Mean Count Rate (counts s^{-1})
SXT	0.5–7.0	9000001276	2017-06-06 15:36:34	2017-06-06 21:06:10	2803	0.357 ± 0.012
		9000001368	2017-07-09 08:33:18	2017-07-09 16:32:50	9565	0.718 ± 0.009
		9000001438	2017-08-07 05:41:13	2017-08-07 13:32:51	8837	0.428 ± 0.007
		9000001524	2017-09-07 18:46:48	2017-09-08 03:35:55	5316	0.247 ± 0.007
		9000001632	2017-10-21 22:03:13	2017-10-22 07:52:31	4591	0.277 ± 0.008
		9000001710	2017-11-22 01:44:24	2017-11-22 05:53:31	3031	0.212 ± 0.009
		9000001754	2017-12-07 22:11:13	2017-12-08 06:50:15	3595	0.247 ± 0.009
		9000002266	2018-08-01 17:31:24	2018-08-01 23:03:30	7063	0.514 ± 0.009
		9000002356	2018-09-11 18:01:33	2018-09-12 02:05:12	8345	0.452 ± 0.008
		9000004598	2021-07-28 01:52:16	2021-07-31 01:54:59	61920	0.257 ± 0.002
		9000004626	2021-08-05 15:09:14	2021-08-07 01:21:42	41190	0.156 ± 0.002
LAXPC	3.0–20.0	9000001276	2017-06-06 15:36:34	2017-06-06 21:06:09	10590	2.633 ± 0.045
		9000001368	2017-07-09 08:50:51	2017-07-09 16:32:50	11940	5.169 ± 0.046
		9000001438	2017-08-07 09:39:31	2017-08-07 13:32:51	10730	2.629 ± 0.045
		9000001524	2017-09-07 19:49:41	2017-09-08 03:35:56	11300	5.255 ± 0.048
		9000001632	2017-10-21 22:50:42	2017-10-22 07:52:31	9616	1.404 ± 0.048
		9000001710	2017-11-22 00:27:27	2017-11-22 05:53:33	11680	2.492 ± 0.045
		9000001754	2017-12-07 23:34:44	2017-12-08 06:50:13	12960	1.661 ± 0.043
		9000002266	2018-08-01 19:08:21	2018-08-01 23:03:30	12670	3.490 ± 0.044
		9000002356	2018-09-11 19:13:45	2018-09-12 02:05:12	12060	2.077 ± 0.046
		9000004598	2021-07-28 01:46:56	2021-07-31 01:55:00	102600	1.496 ± 0.022
		9000004626	2021-08-05 15:09:13	2021-08-07 01:21:42	55860	1.127 ± 0.025
Swift-XRT	0.5–7.0	00035031184 & 00081310002	2020-07-22 02:01:19	2020-07-23 23:02:52	9660	0.379 ± 0.006
		00035031241	2022-08-06 03:58:51	2022-08-06 04:24:53	1556	0.356 ± 0.015
Swift-UVOT	⋯	00035031184 & 00081310002	2020-07-22 02:01:19	2020-07-23 23:02:52	8002	⋯
		00035031241	2022-08-06 03:58:51	2022-08-06 04:24:53	1535	⋯
NuSTAR	3.0–20.0	60160836002	2020-07-22 19:26:09	2020-07-23 07:11:09	20880	0.127 ± 0.003
		80801650002	2022-08-05 18:26:09	2022-08-06 07:11:09	22910	0.075 ± 0.002

Spectroscopic Telescope Array (NuSTAR; Harrison et al. 2013). In addition to these, optical and UV observations are available from the Ultra-violet Optical Telescope (UVOT) onboard Swift. In addition, it was observed in the gamma-ray band by the LAT onboard Fermi (Atwood et al. 2009). In this section, we discuss the details of the observations, data reduction, and data analysis procedures of various instruments. A log of the observations, along with the effective exposure times and the mean count rates in different energy bands, is given in Table 1. The TeV flux measurements, published by the MAGIC team from their 2020 July observations, were utilized in the associated SED modeling.

2.1. AstroSat Observations

AstroSat, the multi-wavelength space observatory launched on 2015 September 28 (Rao et al. 2016) has five scientific payloads which can simultaneously observe objects from optical-UV to hard X-ray energies. These are the Scanning Sky Monitor (Ramadevi et al. 2018), the Ultraviolet Imaging Telescope (Tandon et al. 2017a, 2017b), the SXT (Singh et al. 2016, 2017), the LAXPCs (Yadav et al. 2016; Agrawal et al. 2017), and the Cadmium Zinc Telluride Imager (Rao et al. 2017). 1ES 2344+514 was observed by AstroSat on several occasions from 2017 June to 2021 August, details of which are given in Table 1. We have downloaded publicly available data from SXT and LAXPC for these observations from the Indian Space Science Data Center (ISSDC)[6] and used them in the present work.

2.1.1. SXT Observations

The SXT is a focusing X-ray telescope based on the grazing incidence principle with a focal length of 2 m. It has a

[6] https://astrobrowse.issdc.gov.in/astro_archive/archive/Home.jsp

thermoelectrically cooled CCD in the focal plane, which collects the X-ray photons. Its operational energy range is 0.3–8.0 keV with an energy resolution of 5%–6% at 1.5 keV. 1ES 2344+514 was observed in the photon counting (PC) mode. The raw Level1 (L1) data of individual orbits were received from the satellite to the data acquisition center at the ISSDC and transferred to the SXT Payload Operation Center (POC). Later, X-ray data from individual orbits were reduced to Level2 (L2) data files through SXTPIPELINE (Version:1.4b)[7] at the POC. The task of event generation, time tagging of events above a pre-set threshold and the electronic noise level, the coordinate transformation from the detector to sky coordinates, bias subtraction, flagging of spurious pixels, and calibration of source events were carried out in the pipeline. Event grading (similar to Swift-XRT; see Romano et al. 2005) and removal of the events with grades >12, the event pulse height amplitude (PHA) construction, the conversion from the event PHA to the X-ray energy (Pulse Invariant; PI), and a search and removal of hot and flickering pixels were also involved. Further, the events with a bright Earth-avoidance angle of $\geqslant 110^\circ$ were screened and those data during the passage through the South Atlantic Anomaly were removed using the criteria that the Charged Particle Monitor rate is below 12 counts s^{-1}. Good Time Intervals (GTIs) were constructed and filtered, generating the L2 events files. The science products were generated from L2 event files. The orbit-wise L2 SXT data files were downloaded from the AstroSat archive. The individual orbit L2 data contained cleaned event files. These individual cleaned event files were merged using the Julia package SXTMerger.jl,[8] also available at the SXT website,[9] which takes care of exposure overlapping within GTIs. The merged cleaned event files were compatible with HEASoft software. An image of the cleaned events file was created using DS9 (version 8.3) and from this image, a circular region of 10′ radius and an annular region with a radius extending from 13′ to 19′ centered on the source were chosen as the source and the background region, respectively, based on a radial profile similar to Chaudhury et al. (2018). The XSELECT (version 2.4) tool of HEASOFT (version 6.28) was used to extract the source and background filtered light curves and spectra from the SXT merged cleaned events file. The XSPEC (version: 12.11.1) (Arnaud 1996) compatible ancillary response file (ARF; sxt_pc_excl01_v03.arf), the response matrix file (sxt_pc_mat_g0to12.rmf) and the blank-sky background spectrum file (SkyBkg_comb_EL3p5_Cl_Rd16p0_v01.pha) provided by the SXT team[10] were used for spectral analysis. The spectra from SXT were grouped using GRPPHA (v3.1.0) in such a way that a minimum of 20 counts were contained in each energy bin. The spectra over the energy range 0.5–7.0 keV were fitted using XSPEC (v12.11.1) with an absorbed power-law model

$$dE/dN = k(E/E_0)^{-\Gamma}, \quad (1)$$

where Γ is the photon spectral index; $E_0 = 1$ keV is the pivot energy and k is the normalization. The soft X-ray spectrum is affected by the line-of-sight absorption in the interstellar gas, and this is modeled using the Tuebingen-Boulder Inter-Stellar Medium absorption model (tbabs, Wilms et al. 2000) with neutral hydrogen column density ($N_{\rm H}$) fixed at 1.41×10^{21} cm^{-2} (HI4PI Collaboration et al. 2016).

2.1.2. LAXPC Observations

The LAXPC onboard AstroSat has three identical co-aligned independently operating proportional counter units (LAXPC10, LAXPC20, and LAXPC30) with a broad energy range of 3–80 keV, energy resolution in the 22–60 keV range of about 10%–12%, and a collimator field of view (FOV) of 55′ × 55′. The LAXPC30 was suspected to have undergone a gas leakage resulting in a continuous gain shift (Antia et al. 2017). The LAXPC10 was reported to have problems in background normalization for faint sources such as RE J1034+396 (Chaudhury et al. 2018). Therefore, in the present work, only LAXPC20 data have been used. In Event Analysis (EA) mode, each photon arrival time is recorded with a time resolution of 10 μs and a dead-time of about 42 μs (Yadav et al. 2016; Agrawal et al. 2017; Antia et al. 2017). The effective area of LAXPC20 is $\sim$2000 cm^2 in 5–20 keV. The SXT and LAXPC instruments are misaligned by $\sim$6′,[11] much smaller than the FOV of either instrument. We used EA mode data from LAXPC20 for the timing and spectral analyses of 1ES 2344+514. The laxpcl1 tool of the LAXPC software (LAXPCsoft: version 3.4.4)[12] was used for extracting the light curve and the spectrum of the source and background from L1 EA mode data files. The backshiftv3 tool was used to apply a gain shift to the background spectrum, accounting for gain mismatch between source and background runs and to identify required response files (for details, see Antia et al. 2017). Data from the top layer (L1, L2) of the LAXPC20 detector have been used for all analyses to minimize the detector background effect. The spectra from LAXPC20 were grouped using GRPPHA (v3.1.0) in such a way that a minimum of 20 counts were contained in each energy bin. The spectra were fitted over the energy range 3–20 keV only for LAXPC20 because of poor statistics beyond 20 keV. LAXPC spectra were fitted with the power-law model using XSPEC (v12.11.1). In addition to individual fits, the SXT and LAXPC20 spectra were also jointly fitted to get a better handle on the model parameters by

[7] https://www.tifr.res.in/~astrosat_sxt/index.html
[8] https://github.com/gulabd/SXTMerger.jl
[9] http://astrosat-ssc.iucaa.in/uploads/threadsPageNew_SXT.html
[10] https://www.tifr.res.in/~astrosat_sxt/dataanalysis.html
[11] http://astrosat-ssc.iucaa.in/uploads/APPS/NoteOnRelativeAngleBetwwenPayloads_Astrosat_15072016.pdf
[12] https://www.tifr.res.in/~astrosat_laxpc/LaxpcSoft.html

covering a larger dynamic range of about 0.5–20 keV with a log-parabola model (Massaro et al. 2004) including relative normalization between the SXT and LAXPC20 instruments with a fixed value for neutral hydrogen column density ($N_{\rm H}$) to model line of sight absorption. Relative normalization accounts for cross-calibration between two detectors as well as for the fact that data from these two detectors are not strictly simultaneously coupled with the variable nature of the source. The mathematical form of the log-parabola model is as follows

$$\frac{dN}{dE} = k\left(\frac{E}{E_b}\right)^{-\alpha-\beta\log(E/E_b)}, \tag{2}$$

where α is the photon spectral index at the energy E_b, β is the curvature parameter, k is the normalization, and E_b is the reference energy that was kept fixed at 1 keV during the fitting. The synchrotron peak energy is estimated using the following equation (Massaro et al. 2006)

$$E_p = E_b 10^{(2-\alpha)/2\beta}. \tag{3}$$

The synchrotron peak frequency is obtained in XSPEC using the eplogpar model.

2.2. Swift-XRT Observations

1ES 2344+514 has been observed on various occasions with Swift-XRT (Burrows et al. 2005), the grazing incidence focusing telescope operating in the energy range 0.3–8.0 keV. In this work, we used data that were simultaneous with NuSTAR observations. These data were recorded in PC mode, and obtained from the Swift public archive[13] (see Table 1 for details). All XRT data were processed using the XRTDAS software package (version 3.6.0) available under HEASOFT (version 6.28). The Swift-XRT calibration files (2023 July 25 files) were used within standard Swift XRTPIPELINE (version 0.13.5) for calibrating and cleaning the event files. A circular region of radius 20 pixels centered at R. A. and decl. of the source was chosen as the source region, and a circular region of 40 pixel radius away from the source was chosen as the background region. XRTPRODUCTS (v0.4.2) was used to extract the source and background spectra. The ARFs were generated via the task "xrtmkarf," taking care of corrections for point-spread function losses and CCD defects using the exposure map. XRT spectra obtained from observation IDs 00035031184 and 0081310002 were combined using ADDSPEC (v1.4.0) as they are quasi-simultaneous with NuSTAR observation ID 60160836002. Spectra were grouped using GRPPHA (v3.1.0) with a minimum of 20 counts in each energy bin. Individual spectra in the energy range 0.3–8 keV from Swift-XRT, with proper response, and an ARF were loaded into XSPEC (v12.11.1) and fitted with the power-law model with fixed hydrogen column density, $N_{\rm H} = 1.41 \times 10^{21}$ cm^{-2}. The unabsorbed flux was computed using the cflux convolution model in the energy range of 0.5–7 keV.

2.3. Swift-UVOT Observations

Swift has the capability of getting simultaneous Optical-UV and X-ray observational data. Optical-UV data were obtained from Swift-UVOT (Roming et al. 2005), simultaneous with 2020 July and 2022 August X-ray observations. It has three filters UW1, UM2, and UW2, in the UV band and three filters V, B, and U in the optical band. Swift-UVOT data were analyzed using the tools within the HEASOFT (v6.28) package. The UVOTIMSUM tool was used to integrate all observational data of selected epochs. To estimate flux values from integrated image files for various filters, circular regions with a radius of 5″ and 8″, centered around the source position, were used respectively for visible and UV filters, whereas background flux values were obtained using circular regions with a radius of 25″ located away from the source. The flux magnitudes were extracted using the UVOTSOURCE tool and then corrected for the Galactic extinction of $E(B-V) = 0.1819$ mag (Schlegel et al. 1998) for all filters as obtained using a web tool.[14]

2.4. NuSTAR Observations

NuSTAR (Harrison et al. 2013) is the first focusing high energy X-ray telescope covering the energy range 3–79 keV, launched on 2012 June 13. 1ES 2344+514 was observed on a few occasions with its two co-aligned X-ray telescopes i.e., Focal Plane Module A (FPMA) and B (FPMB). We used publicly available data from the HEASARC archive[15] for two observations carried out in 2020 July and 2022 August, details of which are given in Table 1. The level 1 NuSTAR data were processed using the NUSTARDAS software package (version 2.0.0) available within the HEASOFT package. The latest NuSTAR calibration files (2023 October 17 files) were used within NUPIPELINE (v.0.4.8) for calibrating and cleaning the event files. The spectra of the source for different observations were extracted using NUPRODUCTS (v.0.3.2) with a circle of radius 12 pixels centered on the R.A. and decl. of the source, and the background was chosen from a region away from the source to extract the background spectra. Spectra were grouped using GRPPHA (v3.1.0) with a minimum of 30 counts in each energy bin for FPMA/B onboard NuSTAR. Individual spectra of the FPMA/B in the energy range 3–79 keV, with appropriate response, and ARFs were loaded into XSPEC (v12.11.1) and fitted with the power-law model. The corresponding flux was computed in the energy range 3–20 keV. Similarly, the combined Swift-XRT and NuSTAR FPMA/B spectra were fitted with constant*tbabs*logpar in the broadband X-ray energy range 0.3–79 keV. The

[13] https://swift.gsfc.nasa.gov/archive/

[14] https://ned.ipac.caltech.edu/forms/calculator.html

[15] https://heasarc.gsfc.nasa.gov/docs/archive.html

synchrotron peak frequency is obtained in XSPEC using the eplogpar model.

2.5. Fermi-LAT Observations

The LAT instrument is a pair-production telescope onboard the Fermi satellite launched in 2008 (Atwood et al. 2009; Ackermann et al. 2012). It covers the 20 MeV to 1 TeV energy band with ∼2.3 sr FOV and covers the entire sky every three hours with an orbital period of ∼96 minutes. Fermi-LAT observations of 1ES 2344+514 have been available since 2008. For the multiwaveband study, we have obtained the data from Fermi-LAT data archive[16] in the energy range 30 MeV to 1 TeV from a region of radius 30° centered on the source. The data from 2017 June 6th 15:36:34 to 2022 August 6th 07:11:09 over the energy range of 0.1–500 GeV were analyzed to get γ-ray spectra simultaneous with X-ray observations.

The analysis is performed using the standard software package FERMITOOLS(v1.2.1) supplied by Fermi-LAT collaboration and user-contributed ENRICO Python script (Sanchez & Deil 2013). A circle of radius 10° centered at the source 1ES 2344+514 was considered as the region of interest (ROI) for photon event extraction with evclass = 128 and evtype = 3. GTIs were restricted using the filter "DATA QUAL>0 && LAT CONFIG == 1" as recommended by the Fermi-LAT collaboration.[17] Also, events with zenith angles smaller than 90° were chosen to avoid the contribution from the Earth limb's γ-rays. The galactic interstellar emission model "gll_iem_v07.fits" and isotropic spectral template "iso_P8R3_SOURCE_V3_v1.txt" were used as the diffused background models[18] to take care of background γ-ray emission. The source spectrum is obtained using the binned and unbinned maximum likelihood approach with the instrumental response function P8R3_SOURCE_V3.

The γ-ray light curve and SEDs were extracted from Fermi-LAT data. For this purpose, an XML file was created that contains the spectral information of all the γ-ray sources lying within the radius of 20° (ROI + 10°) centered at 1ES 2344 +514. The spectral parameters of the sources were taken from the fourth Fermi-LAT source catalog Data Release 2 (4FGL-DR2, Abdollahi et al. 2020). All the spectral parameters of the sources within 5° radius of 1ES 2344+514 were left free during the likelihood fitting process. For sources within 5°–10°, all spectral parameters except for normalization were fixed to 4FGL catalog values, whereas for sources within 10°–20°, all parameters were fixed to 4FGL catalog values. The determination of the photon flux and spectral parameters for the source was carried out using a binned and unbinned likelihood analysis method GTLIKE. The likelihood analysis was performed in an iterative manner. Sources with test statistics (TSs) less than 1 were eliminated during each fitting iteration. Log-parabola and PowerLaw2 were used to model the source spectra for different time epochs. The log-parabola model is defined in Equation (2), and the PowerLaw2 model is given as follows

$$\frac{dN}{dE} = \frac{N(\gamma - 1)E^{\gamma}}{E_{\max}^{\gamma+1} - E_{\min}^{\gamma+1}}, \tag{4}$$

where γ is the spectral index, $E_{\min}$ and $E_{\max}$ are the energy bounds and N is the integral flux over the energy range considered. The LAT model fits and the butterfly contours were extended up to the maximum energy of 500 GeV, and the correction for extragalactic background light (EBL) absorption was applied to γ-ray spectra using the model of Franceschini & Rodighiero (2017).

The flux points in the SED unit are estimated by dividing the entire energy range of the source into a few bins. For bins with values of TS < 9 (i.e., $\lesssim 3\sigma$ significance), the flux upper limit is calculated at 95% confidence level using the profile likelihood method.

3. Results

3.1. AstroSat

1ES 2344+514 was observed simultaneously by SXT and LAXPC onboard AstroSat on several occasions, the details of which are given in Table 1. The light curves and spectra were generated for all these observations following the procedure outlined in Sections 2.1.1 and 2.1.2. In addition, the individual and combined spectra of SXT and LAXPC were fitted using the procedure mentioned in Sections 2.1.1 and 2.1.2. The best-fit parameters for individual SXT and LAXPC spectra along with unabsorbed flux are presented in Table 2 for 11 observation epochs during 2017–2021. Figure 1 shows the combined spectral plot for the SXT (0.5–7.0 keV) and LAXPC20 (3–20 keV) observations carried out on 2017 July 9 with the best-fitted log-parabola model. The values of the best-fit parameters along with the peak energy (E_p) and χ^2/dof for the log-parabola model are given in Table 4 for 11 epochs.

MAGIC Collaboration et al. (2024) have carried out a detailed multiwaveband analysis of 1ES 2344+514. They used AstroSat-SXT data observed on 2021 August 6 and fitted the spectrum using a log-parabola model. We also used these data for our spectral analysis. The measured values of the spectral parameters presented in this paper are found to be consistent with those obtained by MAGIC Collaboration et al. (2024) (see their Table 3).

3.2. Swift-XRT and NuSTAR

The nearly-simultaneous X-ray data from Swift-XRT and NuSTAR observations were chosen for this work. The details

[16] https://fermi.gsfc.nasa.gov/ssc/data/access/
[17] https://fermi.gsfc.nasa.gov/ssc/data/analysis/documentation/
[18] http://fermi.gsfc.nasa.gov/ssc/data/access/lat/BackgroundModels.html

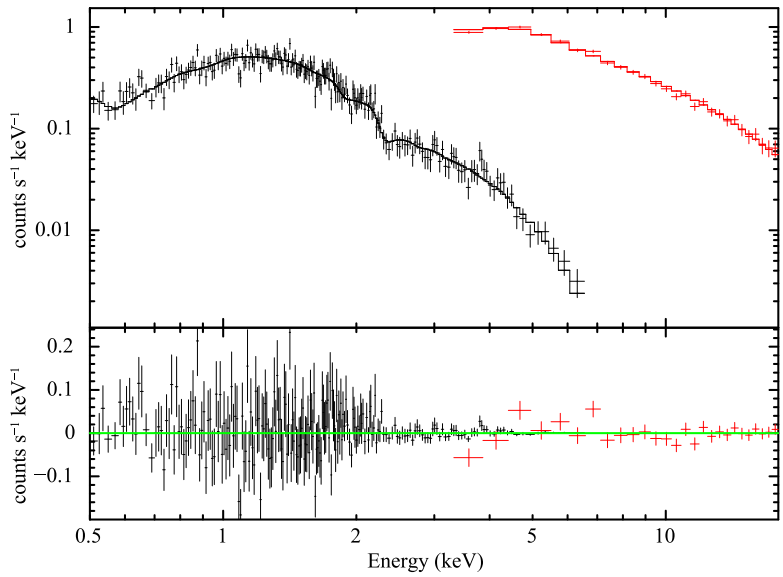

Figure 1. Joint fit for SXT (black) and LAXPC20 (red) spectra for 2017 July 9 observations with the log-parabola model along with the line of sight absorption. Data over energy ranges 0.5–7.0 keV and 3.0–20.0 keV are used for SXT and LAXPC20, respectively. The top panel shows data and model fit, whereas the bottom panel shows the residuals.

Table 2
Best-fit Absorbed Power-law Results for SXT and LAXPC Spectral Analysis

	SXT (0.5–7.0 keV)			LAXPC (3.0–20.0 keV)		
Obs. Date	Γ	Flux [a]	χ^2/dof	Γ	Flux [b]	χ^2/dof
06-06-2017	2.014 ± 0.073	2.887 ± 0.106	45.67/46	2.114 ± 0.041	2.276 ± 0.041	29.59/25
09-07-2017	1.873 ± 0.027	6.013 ± 0.087	199.44/211	2.037 ± 0.021	4.451 ± 0.043	48.13/25
07-08-2017	1.930 ± 0.037	3.502 ± 0.068	158.21/148	2.064 ± 0.042	2.243 ± 0.042	28.48/25
07-09-2017	2.030 ± 0.068	1.945 ± 0.064	71.47/63	2.022 ± 0.022	4.524 ± 0.045	48.67/25
21-10-2017	1.897 ± 0.064	2.322 ± 0.080	53.93/60	2.285 ± 0.092	1.243 ± 0.047	15.09/14
21-11-2017	2.100 ± 0.100	1.688 ± 0.078	29.31/32	2.205 ± 0.047	2.108 ± 0.042	36.76/19
07-12-2017	1.858 ± 0.084	2.065 ± 0.089	54.31/43	2.221 ± 0.068	1.415 ± 0.040	33.9/17
01-08-2018	1.849 ± 0.037	4.311 ± 0.087	157.02/146	2.171 ± 0.031	2.969 ± 0.040	30.05/24
11-09-2018	1.939 ± 0.038	3.699 ± 0.072	140.95/152	2.564 ± 0.055	1.875 ± 0.039	26.55/17
28-07-2021	2.131 ± 0.019	2.058 ± 0.019	342.3/267	2.366 ± 0.030	1.258 ± 0.019	40.59/25
05-08-2021	2.130 ± 0.034	1.234 ± 0.020	248.37/214	2.280 ± 0.058	0.936 ± 0.022	37.88/23

Notes.
[a] Unabsorbed Flux in units of 10^{-11} erg cm^{-2} s^{-1} in 0.5–7 keV energy range.
[b] Flux in units of 10^{-11} erg cm^{-2} s^{-1} in 3–20 keV energy range.

of the observations are listed in Table 1. The combined and individual spectral fitting for both instruments was discussed in Sections 2.2 and 2.4.

The best-fitted spectral parameters along with unabsorbed flux are tabulated in Table 3 for two observation epochs, 2020 July 22 and 2022 August 5. The results of the combined fit parameters are listed in Table 4. Figure 2 shows the combined best-fitted spectral plot for the Swift-XRT (0.3–8.0 keV) and NuSTAR-FPMA/B (3–79 keV) for 2020 July 22 observations. The constant component in the fitted model corresponds to the relative normalization between Swfit-XRT and NuSTAR FPMA/B, and the corresponding best-fitted peak energy (E_p) is listed in Table 4.

We investigated a correlation between the peak energy of SED (E_p) and corresponding peak flux (S_p) obtained using the log-parabola model. Figure 3 shows the scatter plot of the peak energy of SED versus the corresponding peak flux along with the fitted weighted and mean bootstrapped regression lines. A

Table 3
Best-fit Absorbed Power-law Results for Swift-XRT and NuSTAR Spectral Analysis

	Swift-XRT (0.3–8 keV)			NuSTAR-FPMA (3–79 keV)			NuSTAR-FPMB (3–79 keV)		
Obs. Date	Γ	Flux [a]	χ^2/dof	Γ	Flux [b]	Chi^2/DOF	Γ	Flux [b]	χ^2/dof
22–07–2020	2.025 ± 0.029	1.834 ± 0.032	129.66/140	2.318 ± 0.045	1.254 ± 0.025	57.48/72	2.293 ± 0.046	1.291 ± 0.026	80.17/72
05–08–2022	2.096 ± 0.082	1.682 ± 0.075	29.13/24	2.469 ± 0.059	0.769 ± 0.019	50.86/49	2.422 ± 0.058	0.865 ± 0.021	48.8/51

Notes.
[a] Unabsorbed Flux in units of 10^{-11} erg cm^{-2} s^{-1} in 0.5–7 keV energy range.
[b] Flux in units of 10^{-11} erg cm^{-2} s^{-1} in 3–20 keV energy range.

Table 4
Results of Joint SXT-LAXPC and XRT-NuSTAR Spectral Fit with constant*tbabs*logpar Model

Instruments	Obs. Date	α	β	Peak Energy (E_p)	Constant[a]	Flux [b]	χ^2/dof
SXT and LAXPC	06-06-2017	1.905 ± 0.097	0.142 ± 0.067	2.163 ± 1.021	1.187 ± 0.086	1.730 ± 0.107	71.9/75
	09-07-2017	1.780 ± 0.037	0.155 ± 0.029	4.450 ± 0.642	0.998 ± 0.032	3.851 ± 0.097	224.9/236
	07-08-2017	1.876 ± 0.051	0.119 ± 0.043	3.320 ± 0.904	0.909 ± 0.041	2.162 ± 0.076	186.45/176
	07-09-2017	1.925 ± 0.083	0.069 ± 0.052	3.484 ± 1.846	3.206 ± 0.195	1.218 ± 0.065	116.47/88
	21-10-2017	1.637 ± 0.100	0.487 ± 0.103	2.361 ± 0.318	0.903 ± 0.074	1.343 ± 0.084	54.64/74
	21-11-2017	2.010 ± 0.134	0.130 ± 0.091	0.913 ± 1.138	2.145 ± 0.211	0.929 ± 0.078	64.86/50
	07-12-2017	1.640 ± 0.120	0.398 ± 0.097	2.834 ± 0.488	1.059 ± 0.093	1.257 ± 0.089	78.24/60
	01-08-2018	1.732 ± 0.052	0.272 ± 0.040	3.106 ± 0.335	1.020 ± 0.041	2.658 ± 0.089	184.23/170
	11-09-2018	1.737 ± 0.058	0.517 ± 0.058	1.796 ± 0.152	1.079 ± 0.052	1.885 ± 0.070	169.26/169
	28-07-2021	2.016 ± 0.027	0.234 ± 0.032	0.924 ± 0.130	1.221 ± 0.036	1.039 ± 0.022	303.94/264
	05-08-2021	2.034 ± 0.047	0.206 ± 0.052	0.826 ± 0.247	1.485 ± 0.072	0.626 ± 0.022	249.6/204
XRT and NuSTAR	22-07-2020	1.850 ± 0.036	0.275 ± 0.034	1.854 ± 0.185	1.241 ± 0.123	1.049 ± 0.031	266.43/297
	05-08-2022	1.988 ± 0.095	0.270 ± 0.061	1.052 ± 0.416	0.948 ± 0.082	0.850 ± 0.060	131.69/132

Notes.
[a] The relative normalization between instruments.
[b] Intrinsic/Unabsorbed Flux in units of 10^{-11} erg cm^{-2} s^{-1} calculated using *Cflux* multiplicative model in energy range 2–10 keV.

positive correlation with the weighted Pearson's correlation coefficient (Fuller 1987; Cheng & Van Ness 1999), $r_w = 0.78 \pm 0.09$, the corresponding p-value $= 1.64 \times 10^{-3}$, and the bootstrap mean correlation coefficient (Efron 1979; Carroll & Ruppert 1988), $r_b = 0.70 \pm 0.09$ is seen between these parameters, indicating that the spectral index hardens and the peak of SED shifts toward higher energies during the flares. This is similar to the behavior of other blazars such as Mrk 501, Mrk 421, and others (Massaro et al. 2004, 2006, 2008; Tramacere et al. 2009) reported earlier.

3.3. X-Ray Flux—Photon Spectral Index Correlation

We used simultaneous or quasi-simultaneous X-ray data between SXT and LAXPC onboard AstroSat and also between Swift-XRT and NuSTAR FPMA/B to study the index hardening/softening from 2017 June 6 to 2022 August 6 observations. We computed the X-ray unabsorbed flux values and the corresponding photon spectral indices using the power-law model, and the results are summarized in Tables 2 and 3. Figure 4 shows the plot of the power-law photon spectral index (Γ) as a function of the X-ray integral flux for AstroSat-SXT and Swift-XRT (0.5–7 keV) and AstroSat-LAXPC and NuSTAR-FPMA/B (3–20 keV). The lower and higher energy data points are fitted separately. We observed a negative correlation between the flux and the Γ for both plots. In this plot, the SXT-XRT data show a negative correlation with the weighted Pearson's correlation coefficient, $r_w = -0.74 \pm 0.07$, the corresponding p-value $= 4.05 \times 10^{-3}$, and the bootstrapped correlation coefficient, $r_b = -0.69 \pm 0.07$. It was fitted with weighted linear regression and bootstrap linear regression with a slope of –0.10. In the same plot, the LAXPC-FMPA/B data also show a negative correlation with the weighted Pearson's correlation coefficient, $r_w = -0.80 \pm 0.04$, the corresponding p-value $= 2.43 \times 10^{-3}$, and the bootstrapped correlation coefficient, $r_b = -0.77 \pm 0.04$. It was

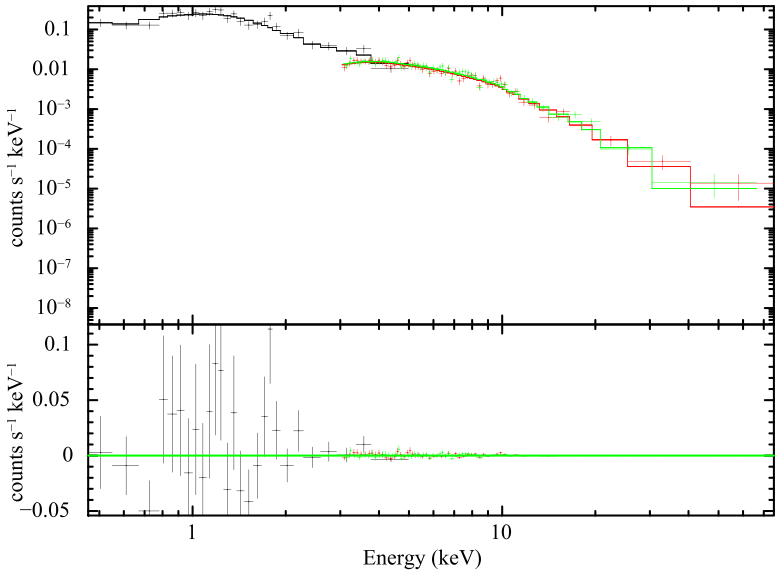

Figure 2. Joint fit for Swift-XRT (black) and NuSTAR FPMA/FPMB (red/green) spectra for 2020 July 22 observations with log-parabola model along with the line of sight absorption. Data over energy ranges 0.3–8 keV and 3–79 keV are used for Swift-XRT and NuSTAR, respectively. The top panel shows data and model fit, whereas the bottom panel shows the residuals.

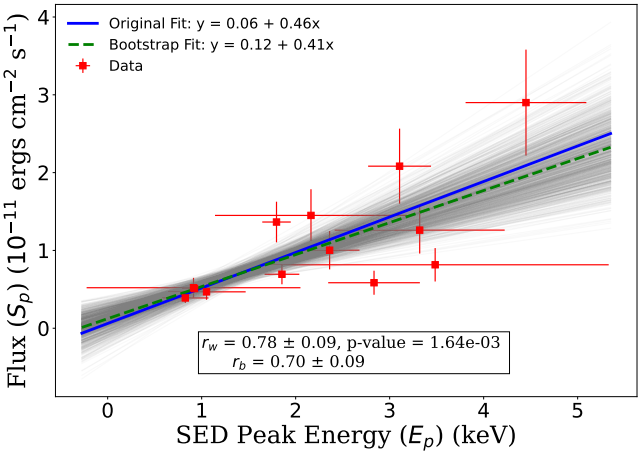

Figure 3. The scatter plot of estimated flux data at the synchrotron peak (S_p) vs. peak energy (E_p) for SXT-LAXPC and XRT-NuSTAR fitted with weighted linear regression and bootstrap linear regression. The gray lines are bootstrapped regression lines, the green dashed line is their mean, and the blue line is the weighted linear regression line.

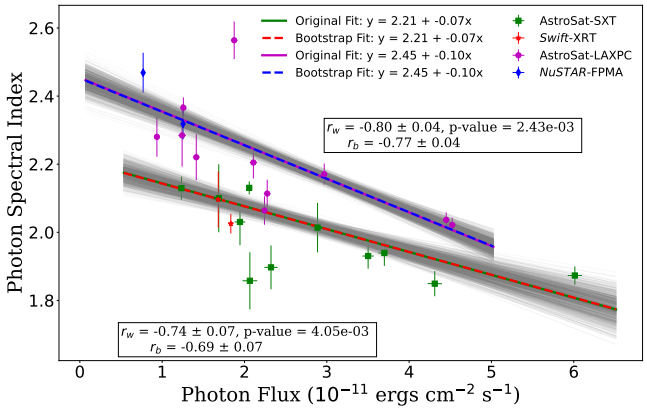

Figure 4. The scatter plot illustrates the relationship between the power-law photon spectral index and X-ray photon flux. Flux values for Swift-XRT and SXT are calculated over the 0.5–7 keV energy range, while LAXPC and NuSTAR cover the 3–20 keV range. These plots are analyzed using weighted linear regression and bootstrap linear regression. Gray lines represent bootstrapped regression lines for both plots. For the SXT-XRT data (bottom), the red dashed line indicates the mean of bootstrapped regression lines, and the green line shows the weighted linear regression. For the LAXPC-FPMA data (top), the blue dashed line represents the mean of bootstrapped regression lines, and the purple line depicts the weighted linear regression.

fitted with weighted linear regression and bootstrap linear regression with a slope of –0.07. This plot shows the "harder-when-brighter" trend in the X-ray energy region. The measured AstroSat-SXT and Swift-XRT Γ values range from 1.85 to 2.13 and the flux varies by a factor of 4.9 over the energy range of 0.5–7 keV. Whereas for AstroSat-LAXPC and NuSTAR-FPMA/B in the energy range 3–20 keV, the Γ varies from 2.02 to 2.56 and the flux varies by a factor of 5.1.

3.4. *Swift-UVOT*

The corrected observed flux magnitudes obtained for various UVOT filters, following the procedure mentioned in Section 2.3, were converted into the fluxes in the SED unit using zero-point magnitudes (Poole et al. 2008). The flux

Table 5
Summary of the Swift-UVOT Data Analysis

Obs Date/Filters	Units	*V*	*B*	*U*	W1	M2	W2
22-07-2020	10^{-11} erg cm^{-2} s^{-1}	2.322 ± 0.076	1.476 ± 0.044	0.853 ± 0.031	0.717 ± 0.031	0.700 ± 0.038	0.602 ± 0.025
05-08-2022	10^{-11} erg cm^{-2} s^{-1}	2.155 ± 0.088	1.432 ± 0.053	0.768 ± 0.037	0.620 ± 0.037	0.697 ± 0.051	0.559 ± 0.031

Note. The fluxes of six UVOT filters are reported.

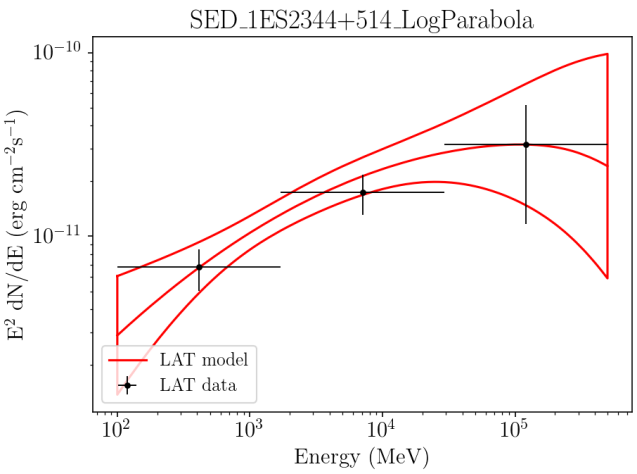

Figure 5. The γ-ray SED, extracted from the Fermi-LAT data observed on 2017 July 9 and fitted with a log parabola model using the binned likelihood fit method with a bin size of 30 days.

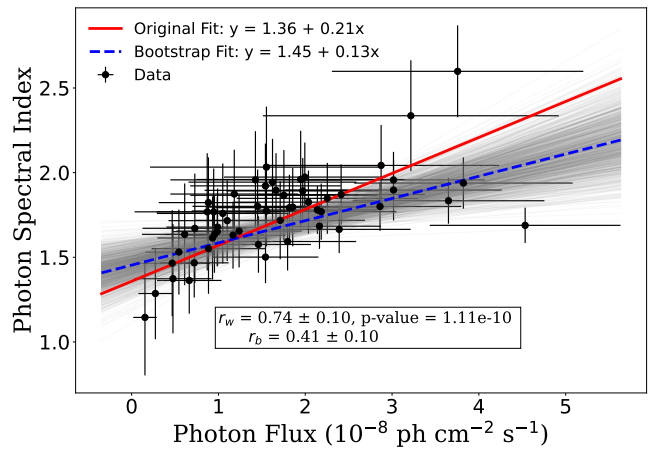

Figure 6. Plot for the correlation between γ-ray photon spectral index vs. flux for 30 day binned Fermi-LAT data. The data were fitted with weighted linear regression and bootstrap linear regression. The gray lines are bootstrapped regression lines, the blue dashed line is their mean, and the red line is the weighted linear regression line.

values obtained for the 2020 July and 2022 August observations for various filters are listed in Table 5.

3.5. Fermi-LAT

The γ-ray Fermi-LAT SED of 2017 July fitted with a log-parabola model is shown in Figure 5. Here Fermi-LAT observation stretches were selected centering on X-ray observation epochs. The observation duration was considered to vary from 30 to 153 days, depending on the γ-ray flux level, to achieve good statistics.

The γ-ray light curve is extracted using the aforementioned likelihood analysis method on the LAT data divided into monthly time bins using the power-law model (see the bottom panel of Figure 7). Also, the flux-Γ correlation for γ-ray data has been studied. Figure 6 shows the photon flux versus Γ plot fitted with weighted linear regression and bootstrap linear regression. A positive correlation between photon flux and Γ is observed with weighted Pearson's correlation coefficient, $r_w = 0.74 \pm 0.10$, the corresponding p-value $= 1.11 \times 10^{-10}$, and the bootstrapped correlation coefficient, $r_b = 0.41 \pm 0.10$ in γ-rays. The trend follows the weighted linear regression line with a slope of 0.21, and the bootstrap mean linear regression line with a slope of 0.13, indicating a "softer-when-brighter" trend.

3.6. Multiwavelength Light Curves

The multiwavelength light curves from 2017 June 6 to 2022 August 6 spanning the X-ray and γ-ray bands are shown in Figure 7. The top panel of the figure displays observation-wise averaged Swift-XRT and AstroSat-SXT fluxes in the 0.3–3.0 keV energy range. The middle panel shows the NuSTAR and LAXPC fluxes in the energy range of 3.0–20 keV for various observations. In the lowermost panel, the Fermi-LAT fluxes in the 0.1–500 GeV energy band are plotted with monthly time binning, as shown by black marks, and the upper limits are shown using gray marks. A bright flare was observed by SXT and LAXPC onboard AstroSat on 2017 July 9 with a simultaneous increase in Fermi-LAT flux. The source was reported to be in a flaring state in VHE γ-rays by MAGIC during 2020 July and 2021 August. The epochs correspond to 30 days or longer duration of Fermi-LAT observational windows centered around X-ray observations. The epochs are marked as vertical yellow shaded areas in Figure 7. Variability is seen in all X-ray and γ-ray light curves.

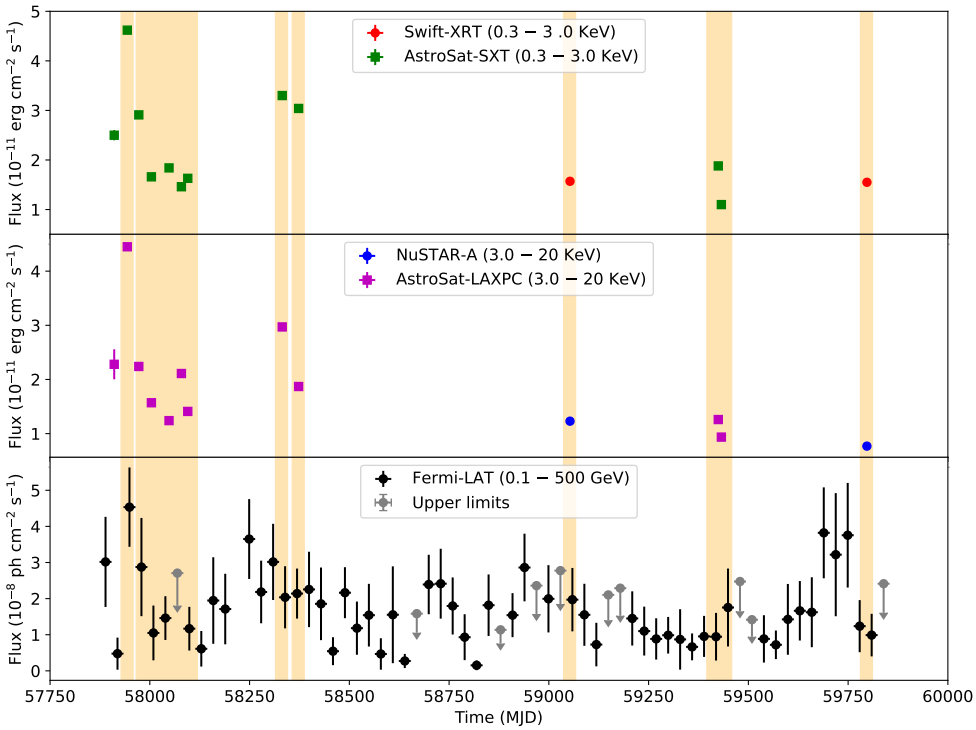

Figure 7. Multiwavelength light curves of 1ES 2344+514 between 2017 June 6 and 2022 August 6. The top panel shows the Swift-XRT (red) and AstroSat-SXT (green) fluxes in 0.3–3.0 keV. The second panel from the top displays the NuSTAR-FPMA (blue) and AstroSat-LAXPC (cyan) fluxes in the energy range of 3.0–20 keV. The third panel from the top represents the Fermi-LAT (black) fluxes in the 0.1–500 GeV energy band with 30 day binning and the upper limits. Yellow shaded areas correspond to epochs for which SEDs are generated.

4. Broadband Spectral Energy Distributions

To study the evolution of multiwaveband SEDs with time and to understand underlying emission mechanisms, SEDs were generated for various epochs, where X-ray observations are available. The epochs with quasi-simultaneous X-ray and gamma-ray observations are marked with yellow shaded areas (see Figure 7). Multiwaveband SEDs were generated and studied for these epochs, typically using the Fermi-LAT data with a duration of 30 days. In the case of low-flux γ-rays, longer duration data, for example, 62 days or 153 days, have been used while generating SEDs.

Two examples of broadband SEDs are shown in Figures 8 and 9. The SED shown in Figure 8 corresponds to the 2020 July epoch and is based on data from Swift-UVOT, Swift-XRT, NuSTAR, Fermi-LAT, and MAGIC. This corresponds to the quiescent state of the source. We have included TeV flux measurements published by the MAGIC Collaboration et al. (2024) in Figure 8. In the present analysis, we have used Swift-XRT data instead of XMM-Newton data used by the MAGIC Collaboration et al. (2024). Also, we do not have VHE data for all of our SEDs. The SED shown in Figure 9 corresponds to the 2017 July epoch and is based on data from AstroSat-SXT, AstroSat-LAXPC, and Fermi-LAT. This epoch corresponds to one of the brightest states of 1ES 2344+514 in the X-ray band. Similar SEDs have also been generated for other epochs. Each SED is fitted with a one zone synchrotron+SSC model including a gamma-ray EBL absorption by the model of Franceschini & Rodighiero (2017). The re-absorption of the synchrotron radiation by the synchrotron electrons themselves (synchrotron self-absorption) at low frequencies below $\approx 10^{12}$ Hz is considered in this model. Archival SED data points (faded yellow) are retrieved from SSDC[19] and used for comparison (Figures 8 and 9). A comparative study between archive data and SEDs from different epochs of the source shows that the source was in its flaring state close to 2017 July 9, as can be seen from the X-ray light curves in Figure 7. To constrain the physical properties of the source 1ES 2344+514, the single-zone leptonic scenario is used to model the emission with the publicly available numerical code JETSE (V1.3.0) provided by Andrea Tramacere (Massaro et al. 2006; Tramacere et al. 2009, 2011; Tramacere 2020). In synchrotron+SSC models, the synchrotron photons produced in the magnetic field (B) get up-scattered by the relativistic electrons. The model assumes that the broadband emission originated from a spherical zone (blob) of radius (R), filled with relativistic electrons accelerated by an isotropic magnetic field. The population of electrons is modeled with a broken

[19] https://tools.ssdc.asi.it/SED/

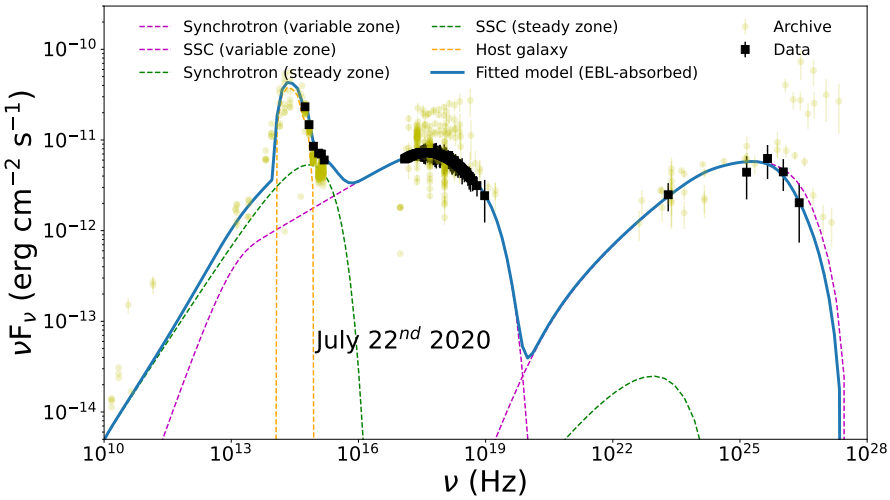

Figure 8. Broadband SED of Swift-UVOT, Swift-XRT, NuSTAR, Fermi-LAT, and MAGIC observations during 2020 July (fainter state) fitted with a two-zone synchrotron+SSC model along with host galaxy component, and archival data shown as yellow points.

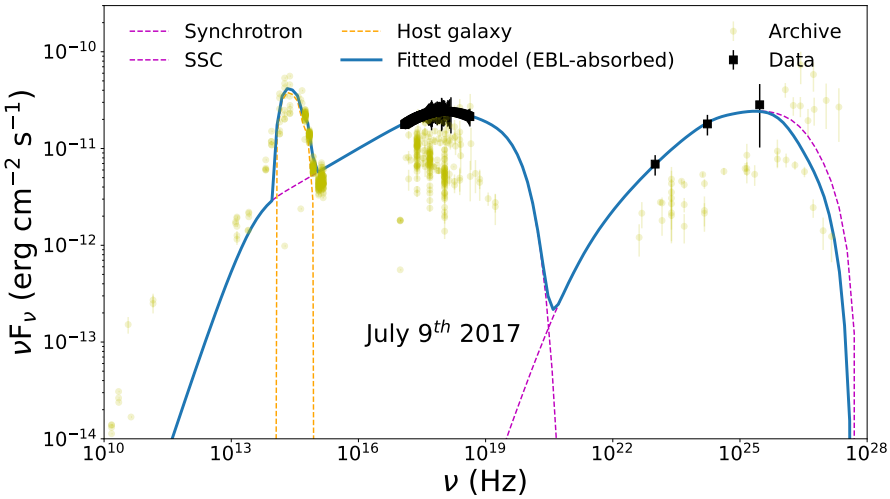

Figure 9. Broadband SED of SXT and LAXPC onboard AstroSat and Fermi-LAT observations during 2017 July (brightest state) fitted with a one-zone synchrotron +SSC model along with host galaxy component. Black points represent the analyzed flux measurement for the selected epochs, and yellow points represent the archived data from the earlier studies.

power-law energy distribution,

$$N(\gamma)d\gamma \propto \begin{cases} K\gamma^{-p_1}d\gamma & \gamma_{\rm min} \leqslant \gamma \leqslant \gamma_{\rm break} \\ K\gamma_{\rm break}^{(p_2-p_1)}\gamma^{-p_2}d\gamma & \gamma_{\rm break} < \gamma \leqslant \gamma_{\rm max} \end{cases}, \quad (5)$$

where K is the normalization constant which corresponds to the electron energy density, denoted as $U_{\rm e}$. Here, p_1 and p_2 are the particle spectral indices below and above the break at energy $\gamma_{\rm break}$ respectively. Also, $\gamma_{\rm min}$, $\gamma_{\rm break}$ and $\gamma_{\rm max}$ are the minimum, break, and maximum Lorentz factors of the injected electron population, respectively. The size of the emission region (R) and the position of the region ($R_{\rm H}$) are set to 2×10^{16} cm and 10^{17} cm, respectively. The fitted SED parameters of the one-zone synchrotron+SCC model for all the epochs are listed in Table 6.

The SED, consisting of X-ray and gamma-ray data, could be fitted with a single-zone synchrotron+SSC model. However, the SED with optical-UV data could not be fitted satisfactorily just with a combination of single zone synchrotron+SSC and host galaxy, as seen by us and as seen by the MAGIC Collaboration et al. (2024) earlier, due to excess emission in UV. To account for this UV excess, following the MAGIC

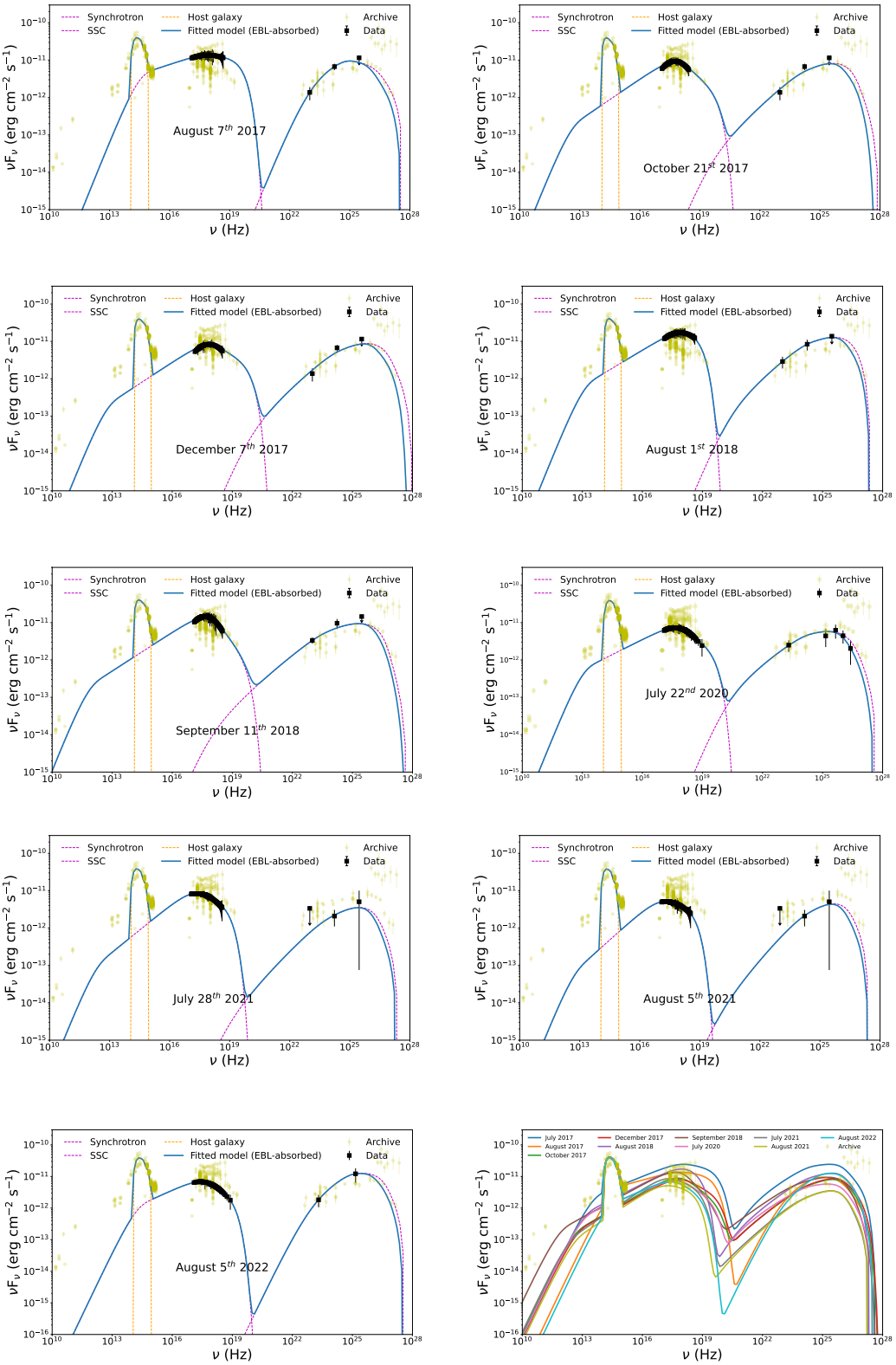

Figure 10. The nine SEDs fitted with one-zone synchrotron+SSC model for each epoch along with data from SXT and LAXPC onboard AstroSat, Swift-XRT, NuSTAR, Fermi-LAT, and MAGIC during 2017 June 6 to 2022 August 6 and host galaxy component are shown in separate panels. Bottom-right panel shows the plot of the fitted broadband SED model of the ten different epochs in a single panel for comparison, and here, 1ES 2344+514 is observed in its brightest state during 2017 July.

Table 6
Best-fit Parameters of the One-zone Synchrotron+SSC Model for Observed SEDs

Obs Date	B (10^{-2} G)	N_e (cm^{-3})	p_1	p_2	$\gamma_{\rm min}$ (10^3)	$\gamma_{\rm max}$ (10^6)	$\gamma_{\rm break}$ (10^5)	U_e (erg cm^{-3})	U_B (erg cm^{-3})	$\eta = U_B/U_e$
					Inner Zone					
09-07-2017	$5.10^{+1.92}_{-1.15}$	$1.03^{+0.24}_{-0.14}$	$2.51^{+0.01}_{-0.01}$	$3.31^{+0.87}_{-0.25}$	$3.66^{+0.52}_{-0.57}$	$6.47^{+5.90}_{-2.62}$	$6.88^{+3.52}_{-1.43}$	9.12×10^{-3}	9.93×10^{-5}	1.09×10^{-2}
07-08-2017	$5.40^{+1.23}_{-0.80}$	$0.17^{+0.05}_{-0.04}$	$2.66^{+0.14}_{-0.10}$	$3.26^{+0.74}_{-0.17}$	$11.4^{+3.42}_{-2.24}$	$5.67^{+3.87}_{-1.60}$	$6.28^{+6.16}_{-1.76}$	3.91×10^{-3}	1.14×10^{-4}	2.92×10^{-2}
21-10-2017	$2.38^{+0.70}_{-0.37}$	$1.57^{+0.32}_{-0.35}$	$2.30^{+0.08}_{-0.08}$	$4.28^{+0.48}_{-0.44}$	$1.88^{+0.56}_{-0.35}$	$5.92^{+3.88}_{-2.43}$	$9.90^{+1.20}_{-1.26}$	9.16×10^{-3}	2.18×10^{-5}	2.39×10^{-3}
07-12-2017	$1.97^{+0.54}_{-0.39}$	$1.33^{+0.27}_{-0.32}$	$2.31^{+0.09}_{-0.08}$	$4.10^{+0.58}_{-0.43}$	$2.55^{+0.89}_{-0.55}$	$8.17^{+6.63}_{-2.99}$	$11.9^{+1.83}_{-2.21}$	1.01×10^{-2}	1.65×10^{-5}	1.64×10^{-3}
01-08-2018	$3.87^{+0.82}_{-0.86}$	$0.95^{+0.22}_{-0.23}$	$2.36^{+0.09}_{-0.09}$	$3.68^{+0.85}_{-0.95}$	$2.92^{+0.76}_{-0.57}$	$2.79^{+2.63}_{-0.99}$	$9.08^{+1.79}_{-2.46}$	7.78×10^{-3}	5.97×10^{-5}	7.67×10^{-3}
11-09-2018	$4.07^{+0.10}_{-0.07}$	$5.42^{+1.16}_{-1.08}$	$2.30^{+0.07}_{-0.06}$	$4.56^{+0.33}_{-0.33}$	$0.59^{+0.15}_{-0.10}$	$4.41^{+2.07}_{-1.43}$	$6.59^{+0.66}_{-0.43}$	1.75×10^{-2}	1.12×10^{-5}	6.41×10^{-4}
22-07-2020	$3.52^{+0.67}_{-0.56}$	$1.11^{+0.29}_{-0.18}$	$2.46^{+0.10}_{-0.08}$	$3.85^{+0.23}_{-0.17}$	$2.53^{+0.48}_{-0.48}$	$7.39^{+6.19}_{-3.25}$	$6.67^{+0.85}_{-0.62}$	6.73×10^{-3}	5.02×10^{-5}	7.46×10^{-3}
28-07-2021	$4.11^{+0.84}_{-0.72}$	$1.04^{+0.26}_{-0.19}$	$2.18^{+0.11}_{-0.12}$	$3.55^{+0.19}_{-0.22}$	$1.11^{+0.24}_{-0.18}$	$2.52^{+0.10}_{-0.46}$	$3.61^{+0.50}_{-0.64}$	4.09×10^{-3}	6.63×10^{-5}	1.56×10^{-2}
05-08-2021	$2.15^{+0.36}_{-0.25}$	$0.53^{+0.14}_{-0.10}$	$2.08^{+0.13}_{-0.06}$	$3.34^{+0.18}_{-0.19}$	$2.76^{+0.64}_{-0.46}$	$2.62^{+0.61}_{-0.37}$	$3.85^{+0.81}_{-0.76}$	5.99×10^{-3}	1.46×10^{-5}	2.44×10^{-3}
05-08-2022	$1.89^{+0.63}_{-0.42}$	$0.25^{+0.08}_{-0.05}$	$2.43^{+0.22}_{-0.14}$	$3.92^{+0.45}_{-0.36}$	$14.5^{+4.32}_{-4.21}$	$5.46^{+7.03}_{-2.04}$	$7.72^{+1.60}_{-1.78}$	8.65×10^{-3}	1.39×10^{-5}	1.61×10^{-3}
					Host Galaxy					
	nuFnu_p_host			erg cm^{-2} s^{-1}			-10.4			
	nu_scale			Hz			-4.2×10^{-3}			

Note. The size of the emission region (R) is set to 2×10^{16} cm and δ to 10.

Collaboration et al. (2024), we have added a second zone to the model so that the entire emission is the sum of contributions from two distinct spatially separated particle populations, along with the host galaxy emission. The second zone, referred to as the "core" zone by the MAGIC Collaboration et al. (2024), contributes mostly in radio with some contribution in the IR/optical/UV part of the spectrum. Whereas, the first zone, referred to as the "variable zone," dominates emission in the optical to the gamma-ray band. The electron distribution in the second-zone component is modeled with the simple power-law function,

$$N(\gamma)d\gamma = K\gamma^{-p}, \ \ \gamma_{\rm min} \leqslant \gamma \leqslant \gamma_{\rm max}, \tag{6}$$

where K is the normalization constant and p is the particle spectral index. This simplified model was adopted due to the sparseness of the radio and optical/UV data. We use the Doppler factor of $\delta = 10$ for both components, which are assumed to be streaming down the jet with the same speed (Hovatta et al. 2009; MAGIC Collaboration et al. 2024). The size of the second zone is set to $R = 10^{17}$ cm, similar to the size of the radio core reported by Aleksić et al. (2013) at 15.4 GHz.

The physical parameters of the second zone, as well as of the first zone, were obtained by fitting the SED for the epoch of 2020 July. The values of the parameters of the second zone are the particle density (N_e) $= 0.23^{+0.20}_{-0.09}$ cm^{-3}, the magnetic field (B) $= 0.22^{+0.09}_{-0.08}$ G, the low-energy spectral slope (p) $= 1.76^{+0.12}_{-0.18}$, the minimum Lorentz factor ($\gamma_{\rm min}$) $= 1.5^{+1.2}_{-0.4}$, and the maximum Lorentz factor ($\gamma_{\rm max}$) $= 1.76^{+0.77}_{-0.46} \times 10^4$. Whereas, the values of parameters of the first zone are the particle density (N_e) $= 1.04^{+0.23}_{-0.15}$ cm^{-3}, the magnetic field (B) $= 3.36^{+0.0.64}_{-0.51} \times 10^{-2}$ G, low energy spectral slope (p_1) $= 2.44^{+0.09}_{-0.04}$, low energy spectral slope (p_2) $= 3.85^{+0.29}_{-0.32}$, the minimum Lorentz factor ($\gamma_{\rm min}$) $= 2.56^{+0.49}_{-0.49} \times 10^3$, the beak Lorentz factor ($\gamma_{\rm break}$) $= 7.70^{+1.15}_{-1.08} \times 10^5$, and the maximum Lorentz factor ($\gamma_{\rm max}$) $= 4.49^{+3.13}_{-1.57} \times 10^6$. The inner zone parameters are quite consistent with the results of MAGIC Collaboration et al. (2024) discussed in their Table 5. It is observed that the contribution of the second zone in X-ray and γ-ray is negligible. In addition, it is difficult to constrain parameters with a two-zone fit with the sparse nature of the data. So, in the rest of the work, we have not considered the second zone, which we refer to as the outer zone, and given results considering the single-zone synchrotron+ SSC model. In Figure 8, the two-component synchrotron+SSC modeling is shown using green dotted lines for emission from the "zone-2" or "outer zone" region and the violet dashed line for emission from the "zone-1" or "inner" region, whereas the blue solid line is the sum of both components along with the host galaxy contribution.

A large part of the flux seen in the optical-UV region ($\sim 10^{14}$–10^{15} Hz), from the archival data of long-term observation of 1ES 2344+514 from SSDC, is due to the stellar emission from the host galaxy of the source. These fluxes are much higher than the non-thermal radiation from the jet. For modeling host galaxy contribution, we have used the archival data points from SSDC, and also the host galaxy component has been added while modeling the SED using JETSET. The host galaxy contribution is shown by the orange dashed lines in Figures 8 and 9. The fits for all broadband SEDs fitted with a one-zone model, for various epochs during

2017 June 6 to 2022 August 6 based on data from SXT and LAXPC onboard AstroSat, Swift-UVOT, Swift-XRT, NuSTAR, Fermi-LAT, and MAGIC, are shown in Figure 10.

The Markov Chain Monte Carlo (MCMC) sampler is performed for all the SEDs to explore all the parameter space of various model components, such as the electron population parameter, magnetic field, the Doppler factor (δ), the electron distribution indices (p_1 and p_2), the break energy ($\gamma_{\rm break}$), etc., using JETSET. We used the corner plot to visualize the marginal posterior distributions of all the parameters, which highlights the uncertainties and parameter degeneracies. The marginal posterior distributions were also used to determine the correlation between the parameters due to degeneracies within the SED spectral fitting. We used 20 walkers with burning initial steps of 50 and a chain length of 500 for MCMC sampling of the one-zone synchrotron+SSC model. The one- and two-dimensional (1D and 2D) marginal posterior distributions for the SED of 2017 July are shown in Figure 11. The median values of the parameters with 68% credible interval are shown above each 1D histogram.

4.1. Jet Power Estimation from SED Modeling

The SED modeling of 1ES 2344+514 provides insights into the jet power, defined in general as the total power carried by the relativistic jet, $P_{\rm jet}$, following Ghisellini & Celotti (2001) and Celotti & Ghisellini (2008), which is

$$P_{\rm jet} = L_e + L_p + L_B + L_{\rm rad}\ ({\rm erg\ s^{-1}}), \tag{7}$$

where L_B, L_p, L_e, and $L_{\rm rad}$ represent the power carried by the magnetic field, cold protons, relativistic electrons, and produced radiation, respectively. The power of each component is calculated as

$$L_i \simeq \pi R^2 \Gamma^2 \beta c U_i, \tag{8}$$

where U_i is the energy density of the ith component in the comoving jet frame, βc is the blob's bulk velocity, Γ is the bulk Lorentz factor, and R is the blob radius. For a jet at angle θ to the line of sight, the Doppler factor is $\delta = [\Gamma(1-\beta\cos\theta)]^{-1}$.

The power carried by relativistic electrons is

$$L_e \simeq \pi R^2 \Gamma^2 \beta c \langle\gamma\rangle N_e m_e c^2, \tag{9}$$

where $\langle\gamma\rangle$ is the average Lorentz factor of electrons in the comoving frame, N_e is the electron number density (an input parameter), and m_e is the electron rest mass. The proton power carried by "cold" protons estimated assuming one proton per relativistic electron, is

$$L_p \simeq \pi R^2 \Gamma^2 \beta c N_p m_p c^2, \tag{10}$$

where $N_p \simeq N_e$ is the proton number density and m_p is the proton rest mass.

The magnetic field power, carried as Poynting flux, is

$$L_B \simeq \frac{1}{8}\pi R^2 \Gamma^2 \beta c B^2, \tag{11}$$

where B is the magnetic field strength in the comoving frame.

The radiative power, associated with non-thermal emission, is

$$L_{\rm rad} = \pi R^2 \Gamma^2 \beta c U_{\rm rad} = L' \frac{\Gamma^2}{4} = L \frac{\Gamma^2}{4\delta^4}, \tag{12}$$

where $U_{\rm rad} = \frac{L'}{4\pi R^2 c}$ is the radiation energy density in the comoving frame, L' is the comoving non-thermal luminosity, and L is the observed total luminosity. The total jet power, $P_{\rm jet}$, and its individual components are calculated within the JETSET framework and the results are presented in Table 7.

5. Discussion

In this work, we report the results of the multi-epoch broadband spectral study along with the light curve of 1ES 2344+514 using the quasi-simultaneous multiwavelength data from 2017 June 6 to 2022 August 6 (MJD 57910–59797). We have carried out a spectral analysis in the energy range of 0.5–7.0 keV for AstroSat-SXT and Swift-XRT, 3–20 keV for AstroSat-LAXPC, 3–79 keV for NuSTAR and optical/UV band for Swift-UVOT observations (Tables 2, 3 and 5). Our study reveals the anti-correlation between the power-law photon spectral index and the integral flux at X-ray energies, as seen in Figure 4. These plots show that the spectrum hardens when the source brightens. This trend is expected in EHSP BL Lacs and is also similar to the results reported earlier (Giommi et al. 2000; Acciari et al. 2011; Aleksić et al. 2013; Kapanadze et al. 2017).

A positive correlation between the γ-ray spectral index and flux has been observed in Figure 6, revealing a "softer-when-brighter" trend in the γ-ray energy range. This trend is expected in HSP BL Lacs. The different trends observed in the X-ray and γ-ray bands are due to the position of the X-ray band at the falling edge of the first hump (synchrotron) and that of the γ-ray band at the rising edge of the second hump (IC) of SED.

A strong correlation is observed between the peak energy (E_p) and the corresponding peak flux (S_p), shown in Figure 3. This trend, where the synchrotron peak shifts to higher energies as the source brightens, is aligned with previous observations by Giommi et al. (2000) and MAGIC Collaboration et al. (2020). Such a displacement of the synchrotron peak between these epochs implies a significant increase in the energy of emitting electrons.

We analyzed the SEDs for epochs where the Astrosat or Swift-UVOT, Swift-XRT, NuSTAR, and MAGIC observations are available, alongside quasi-simultaneous Fermi-LAT data. Initially, a steady-state, one-zone synchrotron+SSC model with a broken power-law electron energy distribution

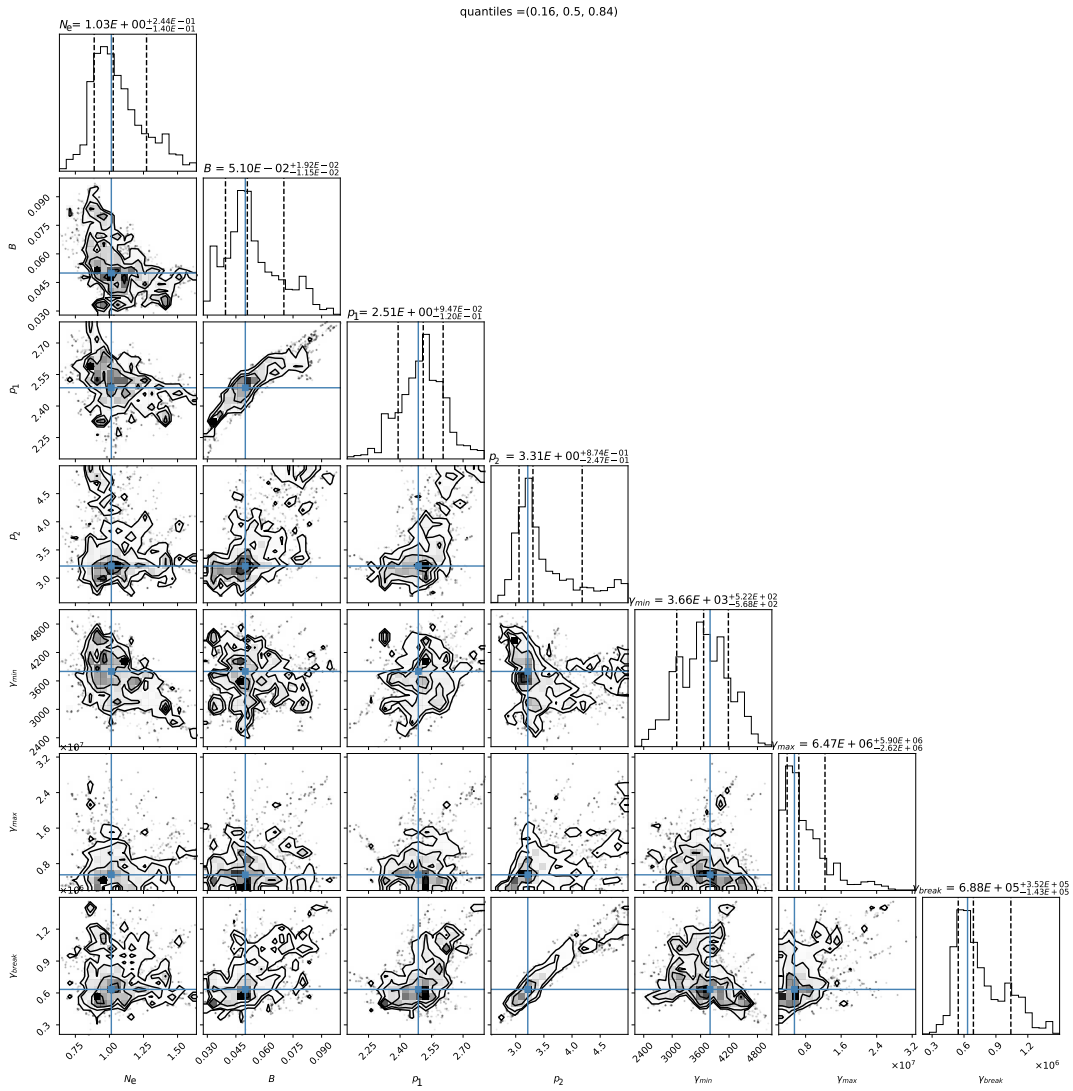

Figure 11. Corner plot of the posterior probability distribution of the free parameters from the SED fit of SXT and LAXPC onboard AstroSat and Fermi-LAT observations during 2017 July fitted with single-zone synchrotron+SSC model. Vertical lines in 1D distributions show 16%, 50%, and 68% quantiles.

Table 7
Jet Power Components and Total Jet Power Derived from Synchrotron+SSC Modeling of 1ES 2344+514's SED for Multiple Observation Dates

Obs. Date	Inner Zone L_e (erg s^{-1})	L_p (erg s^{-1})	L_B (erg s^{-1})	$L_{\rm rad}$ (erg s^{-1})	$P_{\rm jet}$ (erg s^{-1})
09-07-2017	3.42×10^{43}	5.71×10^{42}	3.72×10^{41}	4.61×10^{42}	4.49×10^{43}
07-08-2017	1.47×10^{43}	9.87×10^{41}	4.28×10^{41}	2.14×10^{42}	1.82×10^{43}
21-10-2017	3.43×10^{43}	8.46×10^{42}	8.19×10^{40}	1.36×10^{42}	4.42×10^{43}
07-12-2017	3.78×10^{43}	7.73×10^{42}	6.19×10^{40}	1.40×10^{42}	4.70×10^{43}
01-08-2018	2.92×10^{43}	5.96×10^{42}	2.24×10^{41}	2.32×10^{42}	3.77×10^{43}
11-09-2018	6.55×10^{43}	2.58×10^{43}	4.20×10^{40}	2.52×10^{42}	9.39×10^{43}
22-07-2020	2.21×10^{43}	5.82×10^{42}	1.79×10^{41}	1.13×10^{42}	2.92×10^{43}
28-07-2021	1.53×10^{43}	5.21×10^{42}	2.39×10^{41}	9.08×10^{41}	2.17×10^{43}
05-08-2021	2.25×10^{43}	3.06×10^{42}	5.48×10^{40}	6.87×10^{41}	2.63×10^{43}
05-08-2022	3.24×10^{43}	1.46×10^{42}	5.21×10^{40}	1.42×10^{42}	3.54×10^{43}

was used to fit the broadband SEDs. The fitted parameters, such as particle density (N), magnetic field (B), spectral indices (p_1, p_2), and the Lorentz factors of the minimum ($\gamma_{\rm min}$), break ($\gamma_{\rm break}$), and maximum ($\gamma_{\rm max}$) Lorentz factors, are detailed in Table 6. However, MAGIC Collaboration et al. (2024) reported strong evidence of two separate emitting components contributing to synchrotron emission from the IR to UV wavebands. Similarly, we adopted a two-component model to fit the SEDs for the epochs where the optical-UV data are available. In this framework, the inner zone (zone-1) synchrotron+SSC model, characterized by a broken power-law electron distribution, dominating the X-ray to VHE gamma-ray flux, is filled by highly energetic electrons with $\gamma_{\rm min} \sim (0.59-14.5) \times 10^3$ and $\gamma_{\rm max} \sim (2.52-8.17) \times 10^6$ (see, Table 6). The outer zone synchrotron+SSC model, with a power-law electron energy distribution, primarily accounts for radio emission but also contributes slightly to the IR/optical/UV bands, and it can explain the "UV excess." The electron population corresponding to the outer zone is weaker than that in the inner zone region with $\gamma_{\rm min} \sim 1$ and $\gamma_{\rm max} \sim 10^4$. From Figure 8, it is argued that there is no interaction between the outer and inner zones. The fitted results correspond to the one-zone synchrotron+SSC model discussed here. Figure 9 shows the SED of 1ES 2344+514 with the highest flux in X-rays on 2017 July 7 among the observation epochs considered (Giommi et al. 2000; MAGIC Collaboration et al. 2020), accompanied by elevated γ-ray flux.

In this work, our results show that the maximum Lorentz factor ($\gamma_{\rm max}$) ranges from 2.52×10^6 to 8.17×10^6 across all epochs (see Table 6), which is consistent with the previous results of 1ES 2344+514 (MAGIC Collaboration et al. 2020, 2024). The synchrotron+SSC model reveals a distinct $\gamma_{\rm break}$ between 3.61×10^5 and 11.9×10^5, about an order of magnitude below $\gamma_{\rm max}$. Previous work by Tavecchio et al. (2010) reported that $\gamma_{\rm break}$ lies in the range of 10^4-10^5 during low states for HSP BL Lacs. In addition to the extreme value of $\gamma_{\rm max}$, the low magnetic field between 1.89×10^{-2} and 5.40×10^{-2} G is found to be essential to describe the SEDs. It is also reported that the magnetic field usually lies between 0.1 and 1 G for HSP BL Lacs in the leptonic model (see Tavecchio et al. 2010), but for EHSP BL Lacs the magnetic field is slightly lower, $\sim 10^{-2}-10^{-3}$ G, aligning with our results.

In the synchrotron+SSC model, the first index (p_1), which defines the slope of the electron energy distribution below $\gamma_{\rm break}$, influences the optical and GeV bands through synchrotron and SSC respectively, while the second index (p_2) shapes the X-ray and VHE bands. A very weak correlation is observed between p_1 and p_2, characterized by a weighted Pearson's correlation coefficient of $r_w = 0.30 \pm 0.23$, with a p-value of 0.389, and a bootstrapped correlation coefficient of $r_b = 0.21 \pm 0.23$ (see Figure 12). Notably, the second index (p_2) is much steeper than the expected relation $p_2 = 1 + p_1$, but in a few cases the second index (p_2) is less steep than the expected one, thus the origin of the broken power-law spectrum from the cooling break is ruled out. A weak correlation exists between the first index (p_1) and the bolometric luminosity, with $r_w = 0.56 \pm 0.13$, a p-value of 0.09, and $r_b = 0.42 \pm 0.13$. Similarly, a weak correlation is found between the bolometric luminosity and the particle break energy ($\gamma_{\rm break}$), with $r_w = 0.48 \pm 0.12$, a p-value of 0.16, and $r_b = 0.45 \pm 0.12$ (see Figure 13). Also, a weak correlation is observed between the magnetic field (B) and the bolometric luminosity, with $r_w = 0.72 \pm 0.20$, a p-value of 0.019, and $r_b = 0.65 \pm 0.20$ (see Figure 14).

In our analysis, the magnetization parameter U_B/U_e, where U_B represents the magnetic energy density and U_e the electron energy density, ranges from approximately 6.41×10^{-4} to 2.92×10^{-2}. These values align with previous studies of 1ES 2344+514, which report $U_B/U_e \approx 10^{-3}$ to 10^{-2} (Albert et al. 2007; Tavecchio et al. 2010; Acciari et al. 2011; Aleksić et al. 2013; MAGIC Collaboration et al. 2020). This indicates that the magnetic energy density is significantly lower than the electron energy density, a characteristic commonly observed in BL Lacs during the flaring states. Our findings confirm that the energy equipartition is well below unity, with $U_B/U_e \ll 1$, suggesting a particle-dominated emission region rather than a magnetically dominated one, consistent with results from a select group of EHSP BL Lacs (Costamante et al. 2018), and also for most TeV BL Lacs (Zhang et al. 2012).

In this work (Table 6), we employed a fixed bulk Doppler factor $\delta = 10$ for 1ES 2344+514 following MAGIC Collaboration et al. (2024), due to the absence of simultaneous high-resolution radio observation by VLBI to have a reliable measurement of δ. This value of δ is lower than $\delta \sim 10-35$ reported by Zhang et al. (2012) for their 24 TeV BL Lacs. The magnetic field $B \sim (1.89-5.40) \times 10^{-2}$ G is lower than that of Zhang et al. (2012) 0.1−0.6 G, enabling an extremely high synchrotron peak at $\nu_{\rm sp} \gtrsim 10^{17}$ Hz versus HSP BL Lac peaks at $10^{15}-10^{16}$ Hz. The electron energy density $U_e \sim 3.91 \times 10^{-3}-1.75 \times 10^{-2}$ erg cm^{-3} and magnetization $\eta \sim 6.41 \times 10^{-4}-2.92 \times 10^{-2}$ indicate a jet dominated by particles, more extreme than the values of Zhang et al. (2012). Spectral indices $p_1 \sim 2.08-2.66$, $p_2 \sim 3.26-4.56$ align with Zhang et al. (2012), but a weak correlation between p_1 and p_2 ($r_w = 0.30 \pm 0.23$), Figure 12) suggests non-cooling spectral breaks. Lorentz factors $\gamma_{\rm min} \sim (0.59-14.5) \times 10^3$, $\gamma_{\rm break} \sim (3.61-11.9) \times 10^5$, and $\gamma_{\rm max} \sim (2.52-8.17) \times 10^6$ exceed the ranges of Zhang et al. (2012), driving hard X-ray and VHE γ-ray emission (e.g., 2017 July 7 SED, Figure 9). Lower δ, B, η, and higher $\gamma_{\rm break}$ produce the hard spectra of EHSP, with a "harder-when-brighter" X-ray trend (Figure 4) and synchrotron peak shift (Figure 3), consistent with flaring/quiescent transitions (Tavecchio et al. 2010).

The synchrotron+SSC modeling of 1ES 2344+514's broadband SED (2017–2022) reveals a dynamic particle-dominated jet, with electron power ($L_e \approx 10^{43}-10^{44}$ erg s^{-1})

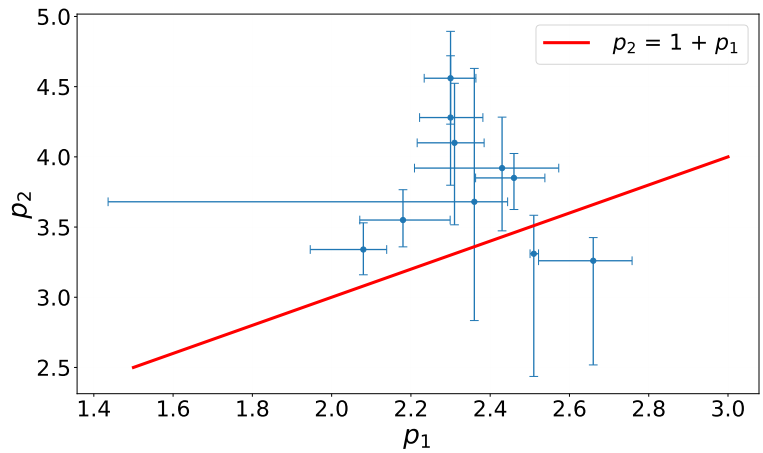

Figure 12. Plot of power-law index of broken power-law used for electron distribution above break energy (p_2) vs. the index below break energy (p_1). The red line corresponds to the relation, $p_2 = 1 + p_1$

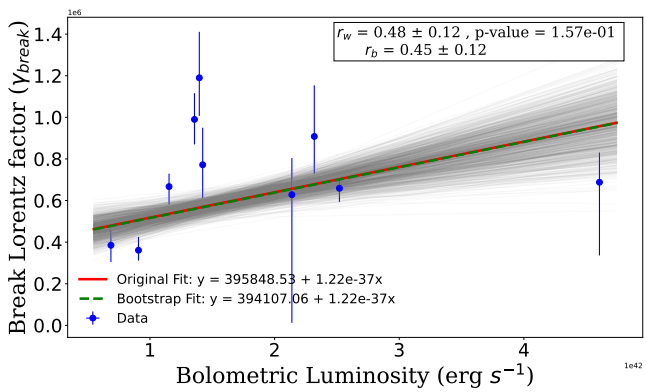

Figure 13. Variation of the break Lorentz factor ($\gamma_{\rm break}$) with total luminosity fitted with weighted linear regression and bootstrap linear regression. The gray lines are bootstrapped regression lines, the green dashed line is their mean, and the red line is the weighted linear regression line.

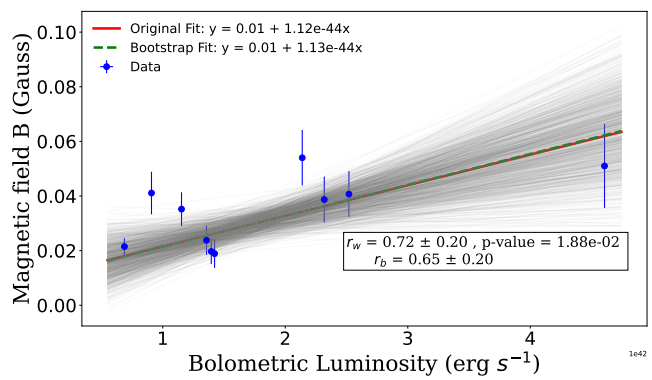

Figure 14. Plot of bolometric luminosity vs. magnetic field in the emission region fitted with weighted linear regression and bootstrap linear regression. The gray lines are bootstrapped regression lines, the green dashed line is their mean , and the red line is the weighted linear regression line.

exceeding both the radiative power ($L_{\rm rad} \approx 10^{42}$ erg s^{-1}) and the magnetic field power ($L_B \approx 10^{41}$ erg s^{-1}). This indicates that the electron power in this BL Lac is sufficient to produce the observed radiation power, estimated from bolometric luminosity. The power carried by the Poynting flux always remains significantly lower than the radiation and electron powers, consistent with the characteristics of an EHSP BL Lac (Costamante et al. 2018). The total jet power ranges from 1.82×10^{43} to 9.39×10^{43} erg s^{-1} (peaking during the 2018 September 11 flare; see, Table 7), dominated by relativistic electrons ($\langle\gamma\rangle$ ranging from 3.936×10^3 to 4.219×10^4, with an average $\langle\gamma\rangle \approx 1.573 \times 10^4$) under the standard one proton per relativistic electron assumption, while low magnetization (an average $\eta \approx 7.96 \times 10^{-3}$) confirms minimal magnetic field contribution. The radiation power ranges from 6.87×10^{41} to 4.61×10^{42} erg s^{-1} (peaking during the 2017 July 9 flare; see, Table 7), and the source appeared in a high state in X-rays and γ-rays with peak flux. The soft X-ray spectrum constrains the synchrotron component, which supports the synchrotron+SSC framework (Tavecchio et al. 2010). The variability in N_e and B across observations suggests evolving jet conditions, potentially linked to the accretion process, or turbulence, shocks, or magnetic reconnection events in the jet (Giannios 2013). Compared to other EHSP BL Lacs, the low magnetization and high jet power of 1ES 2344+514 align with leptonic models, but do not rule out lepto-hadronic contributions (Mannheim 1993; Cerruti et al. 2015).

6. Conclusions

In this study, we have presented the multi-epoch spectral study of 1ES 2344+514 using quasi-simultaneous data. Data in optical, UV, X-ray and γ-ray bands for various epochs

during 2017–2022 from SXT and LAXPC onboard AstroSat, Swift-UVOT, Swift-XRT, NuSTAR and Fermi-LAT and have compared our findings with those of the MAGIC Collaboration et al. (2024) from the 2019–2021 period. The following are our main conclusions.

1. During 2017–2022, the source appeared in a high state in X-rays with peak flux seen on 2017 July 9. This is comparable to the highest flux level seen from this source historically.
2. The X-ray spectra are well fitted with both power-law and log-parabola models. A joint fit between SXT and LAXPC and between Swift-XRT and NuSTAR have been carried out to constrain the location of the synchrotron peak.
3. A clear shift of synchrotron peak is observed across the observation epochs, suggesting an extreme behavior of the source.
4. The source showed spectral evolution such as a "harder-when-brighter" trend in X-rays and a "softer-when-brighter" trend in γ-rays.
5. The broadband SEDs were modeled using a one-zone synchrotron+SSC model, with the electron energy distribution characterized by a broken power-law distribution, yielding results consistent with previous modeling of the object. Additionally, the parameter values derived in our study align closely with those reported by MAGIC Collaboration et al. (2024).
6. Our multiwavelength analysis of 1ES 2344+514 from 2017 to 2022, employing a one-zone synchrotron+SSC model, constrains the jet's physical properties.
7. The magnetic field inside the emission region is also found to be weakly correlated with the bolometric luminosity.
8. There is no significant correlation observed between $\gamma_{\rm break}$ and bolometric luminosity.
9. Jet power calculations, incorporating one proton per relativistic electron, yield ($P_{\rm jet} \approx 10^{43}-10^{44}$ erg s^{-1}), dominated by relativistic electrons (Table 7).
10. The low magnetization (an average $\eta \approx 7.96 \times 10^{-3}$) supports a particle-dominated jet (Costamante et al. 2018), consistent with leptonic synchrotron+SSC models (Tavecchio et al. 2010).
11. Variability in electron density and magnetic field suggests dynamic jet conditions, potentially driven by flaring episodes. Although the synchrotron+SSC model adequately describes broadband emission, hadronic contributions cannot be excluded (Böttcher et al. 2013). Future simultaneous multiwavelength observations, particularly during flares, could further distinguish between leptonic and hadronic processes, refining our understanding of EHSP BL Lac jet physics.

Acknowledgments

This research has used data from the AstroSat mission of the Indian Space Research Organisation (ISRO), archived at the Indian Space Science Data Center (ISSDC). This work has used data from the Soft X-ray Telescope (SXT) developed in a collaboration between the Tata Institute of Fundamental Research (TIFR), Mumbai, India, and the University of Leicester, UK, and the Large X-ray Proportional Counter Array (LAXPC) developed at TIFR, Mumbai, India. The SXT and LAXPC POCs are thanked for verifying and providing the necessary software tools. This research has also made use of the data, software and/or web tools provided by NASA's High Energy Astrophysics Science Archive Research Center (HEASARC), a service of Goddard Space Flight Center (GSFC) and the Smithsonian Astrophysical Observatory. Part of this work is based on archival data, software or online services provided by the ASI (Italian Space Agency) service Data Center (ASDC). The use of XRT Data Analysis Software (XRTDAS) which was developed under the responsibility of ASDC, Italy and the NuSTAR Data Analysis Software (NUSTARDAS), jointly developed by ASDC, Italy and California Institute of Technology (Caltech), USA, is gratefully acknowledged. This study utilized Fermi-LAT data and the Fermitool package, accessed via the Fermi Science Support Center (FSSC), which is provided by NASA. We express our gratitude to Axel Arbet-Engels for supplying the MAGIC data. We acknowledge the support of the Department of Atomic Energy, Government of India, under project identification No. RT4002. This program is supported by Fermi Guest Investigator grants NNX08AN56G, NNX08AN56G, NNX09AV10G, and NNX15AU81G, and a community-developed Python package named ENRICO to make Fermi-LAT data analysis easier and more consistent. We sincerely thank the anonymous reviewer for the thorough reading and constructive feedback.

Data Availability

For this work, we have used data from Fermi-LAT, Swift-XRT, NuSTAR, and SXT and LAXPC onboard AstroSat which are available in the public domain. Links are given as follows:

AstroSat-mission data are available at: https://astrobrowse.issdc.gov.in/astro_archive/archive/Home.jsp.

AstroSat-mission data analysis software package is available at: http://astrosat-ssc.iucaa.in/data_and_analysis and http://astrosat-ssc.iucaa.in/uploads/threadsPageNew_SXT.html.

Swift-mission data are available at: https://heasarc.gsfc.nasa.gov/docs/archive.html.

Swift-mission data analysis software package is available at: https://heasarc.gsfc.nasa.gov/lheasoft/download.html and https://swift.gsfc.nasa.gov/analysis/.

NuSTAR-mission data are available at: https://heasarc.gsfc.nasa.gov/docs/archive.html.

NuSTAR-mission data analysis software package is available at: https://heasarc.gsfc.nasa.gov/lheasoft/download.html and https://heasarc.gsfc.nasa.gov/docs/nustar/analysis/.

Fermi-LAT data are available at: https://fermi.gsfc.nasa.gov/ssc/data/access/.

Fermi-LAT data analysis software is available at: https://fermi.gsfc.nasa.gov/ssc/data/analysis/software/.

SSDC (ASI) archive: https://www.ssdc.asi.it/.

Software for Broadband SED modeling is available at: https://github.com/andreatramacere/jetset.

ORCID iDs

Kishor Chaudhury https://orcid.org/0000-0002-9738-8528

References

Abdo, A. A., Ackermann, M., & Agudo, I. 2010a, ApJ, 716, 30
Abdo, A. A., Ackermann, M., Ajello, M., et al. 2010b, ApJ, 710, 810
Abdo, A. A., Ackermann, M., Ajello, M., et al. 2010c, ApJ, 710, 1271
Abdollahi, S., Acero, F., & Ackermann, M. 2020, ApJS, 247, 33
Acciari, V. A., Aliu, E., & Arlen, T. 2011, ApJ, 738, 169
Acciari, V. A., Aliu, E., Arlen, T., et al. 2010, ApJL, 715, L49
Ackermann, M., Ajello, M., & Albert, A. 2012, ApJS, 203, 4
Ackermann, M., Ajello, M., Allafort, A., et al. 2011, ApJ, 743, 171
Ackermann, M., Ajello, M., Atwood, W. B., et al. 2015, ApJ, 810, 14
Agrawal, P. C., Yadav, J. S., & Antia, H. M. 2017, JApA, 38, 30
Aharonian, F. 2000, NewA, 5, 377
Aharonian, F., Akhperjanian, A. G., Bazer-Bachi, A. R., et al. 2007, A&A, 470, 475
Albert, J., Aliu, E., & Anderhub, H. 2007, ApJ, 662, 892
Aleksić, J., Antonelli, L. A., & Antoranz, P. 2013, A&A, 556, A67
Allen, C., Archambault, S., & Archer, A. 2017, MNRAS, 471, 2117
Antia, H. M., Yadav, J. S., & Agrawal, P. C. 2017, ApJS, 231, 10
Arnaud, K. A. 1996, in ASP Conf. Ser. 101, Astronomical Data Analysis Software and Systems V, ed. G. H. Jacoby & J. Barnes (San Francisco, CA: ASP), 17
Atwood, W. B., Abdo, A. A., & Ackermann, M. 2009, ApJ, 697, 1071
Barth, A. J., Ho, L. C., & Sargent, W. L. W. 2003, ApJ, 583, 134
Blandford, R. D., & Königl, A. 1979, ApJ, 232, 34
Böttcher, M. 2007, Ap&SS, 309, 95
Böttcher, M., Reimer, A., Sweeney, K., & Prakash, A. 2013, ApJ, 768, 54
Burrows, D. N., Hill, J. E., & Nousek, J. A. 2004, Proc. SPIE, 5165, 201
Burrows, D. N., Hill, J. E., & Nousek, J. A. 2005, SSRv, 120, 165
Carroll, R. J., & Ruppert, D. 1988, Transformation and Weighting in Regression (New York: Chapman and Hall/CRC)
Catanese, M., Akerlof, C. W., & Badran, H. M. 1998, ApJ, 501, 616
Celotti, A., & Ghisellini, G. 2008, MNRAS, 385, 283
Cerruti, M., Zech, A., Boisson, C., & Inoue, S. 2015, MNRAS, 448, 910
Chaudhury, K., Chitnis, V. R., & Rao, A. R. 2018, MNRAS, 478, 4830
Cheng, C.-L., & Van Ness, J. W. 1999, Statistical Regression with Measurement Error, Kendall's Advanced Theory of Statistics (London: Arnold)
Costamante, L., Bonnoli, G., & Tavecchio, F. 2018, MNRAS, 477, 4257
Costamante, L., Ghisellini, G., & Giommi, P. 2001, A&A, 371, 512
Dermer, C. D., & Schlickeiser, R. 1993, ApJ, 416, 458
Efron, B. 1979, AnSta, 7, 1
Elvis, M., Plummer, D., Schachter, J., & Fabbiano, G. 1992, ApJS, 80, 257
Fan, Z., Cao, X., & Gu, M. 2006, ApJ, 646, 8
Franceschini, A., & Rodighiero, G. 2017, A&A, 603, A34
Fuller, W. A. 1987, Measurement Error Models (New York: Wiley)
Ghisellini, G., & Celotti, A. 2001, MNRAS, 327, 739
Ghisellini, G., Maraschi, L., & Tavecchio, F. 2009, MNRAS, 396, L105
Ghisellini, G., Tavecchio, F., Foschini, L., et al. 2010, MNRAS, 402, 497
Giannios, D. 2013, MNRAS, 431, 355
Giommi, P., Padovani, P., & Perlman, E. 2000, MNRAS, 317, 743
Godambe, S. V., Rannot, R. C., & Baliyan, K. S. 2007, JPhG, 34, 1683
Goswami, P., Zacharias, M., Zech, A., et al. 2024, A&A, 682, A134
Harrison, F. A., Craig, W. W., & Christensen, F. E. 2013, ApJ, 770, 103
HI4PI Collaboration, Ben Bekhti, N., & Flöer, L. 2016, A&A, 594, A116
Hovatta, T., Valtaoja, E., Tornikoski, M., & Lähteenmäki, A. 2009, A&A, 494, 527
Kapanadze, S., Kapanadze, B., & Romano, P. 2017, Ap&SS, 362, 196
Krawczynski, H., Hughes, S. B., Horan, D., et al. 2004, ApJ, 601, 151
MAGIC Collaboration, Abe, H., Abe, S., & Acciari, V. A. 2024, A&A, 682, A114
MAGIC Collaboration, Acciari, V. A., Ansoldi, S., & Antonelli, L. A. 2020, MNRAS, 496, 3912
Mannheim, K. 1993, A&A, 269, 67
Maraschi, L., Ghisellini, G., & Celotti, A. 1992, ApJL, 397, L5
Massaro, E., Perri, M., Giommi, P., Nesci, R., & Verrecchia, F. 2004, A&A, 422, 103
Massaro, F., Tramacere, A., & Cavaliere, A. 2008, A&A, 478, 395
Massaro, E., Tramacere, A., & Perri, M. 2006, A&A, 448, 861
Mücke, A., & Protheroe, R. J. 2001, APh, 15, 121
Nilsson, K., Lindfors, E., & Takalo, L. O. 2018, A&A, 620, A185
Padovani, P., Alexander, D. M., Assef, R. J., et al. 2017, A&ARv, 25, 2
Perlman, E. S., Stocke, J. T., & Schachter, J. F. 1996, ApJS, 104, 251
Poole, T. S., Breeveld, A. A., Page, M. J., et al. 2008, MNRAS, 383, 627
Ramadevi, M. C., Ravishankar, B. T., & Sarwade, A. R. 2018, JApA, 39, 11
Rao, A. R., Bhattacharya, D., Bhalerao, V. B., Vadawale, S. V., & Sreekumar, S. 2017, CSci, 113, 595
Rao, A. R., Singh, K. P., & Bhattacharya, D. 2016, arXiv:1608.06051
Romano, P., Cusumano, G., & Campana, S. 2005, Proc. SPIE, 5898, 369
Roming, P. W., Kennedy, T. E., Mason, K. O., et al. 2005, SSRv, 120, 95
Sanchez, D. A., & Deil, C. 2013, in 33rd Int. Cosmic Ray Conf. 33 *(Rio de Janeiro, Brazil, 2-9 July 2013)* ed. A. Saa, 2784
Schlegel, D. J., Finkbeiner, D. P., & Davis, M. 1998, ApJ, 500, 525
Schroedter, M., Badran, H. M., & Buckley, J. H. 2005, ApJ, 634, 947
Sikora, M., Begelman, M. C., & Rees, M. J. 1994, ApJ, 421, 153
Singh, K. P., Stewart, G. C., & Chandra, S. 2016, Proc. SPIE, 9905, 99051E
Singh, K. P., Stewart, G. C., & Westergaard, N. J. 2017, JApA, 38, 29
Singh, K. P., Tandon, S. N., & Agrawal, P. C. 2014, Proc. SPIE, 9144, 91441S
Tandon, S. N., Hutchings, J. B., & Ghosh, S. K. 2017a, JApA, 38, 28
Tandon, S. N., Subramaniam, A., & Girish, V. 2017b, AJ, 154, 128
Tavecchio, F., & Ghisellini, G. 2016, MNRAS, 456, 2374
Tavecchio, F., Ghisellini, G., & Ghirlanda, G. 2010, MNRAS, 401, 1570
Tramacere, A., 2020 JetSeT: Numerical Modeling and SED Fitting Tool for Relativistic Jets, Astrophysics Source Code Library, ascl:2009.001
Tramacere, A., Giommi, P., & Massaro, E. 2007, A&A, 467, 501
Tramacere, A., Giommi, P., Perri, M., Verrecchia, F., & Tosti, G. 2009, A&A, 501, 879
Tramacere, A., Massaro, E., & Taylor, A. M. 2011, ApJ, 739, 66
Urry, C. M., & Padovani, P. 1995, PASP, 107, 803
Wilms, J., Allen, A., & McCray, R. 2000, ApJ, 542, 914
Yadav, J. S., Agrawal, P. C., & Antia, H. M. 2016, Proc. SPIE, 9905, 99051D
Zhang, J., Liang, E.-W., Zhang, S.-N., & Bai, J. M. 2012, ApJ, 752, 157
Zhang, J., Sun, X.-N., Liang, E.-W., et al. 2014, ApJ, 788, 104